Gravity currents over topography in a two-layer ambient

by

Mitchell Nicholson

A thesis submitted in partial fulfillment of the requirements for the degree of

Master of Science

Department of Mechanical Engineering
University of Alberta

Abstract

A total of 95 full- and partial-depth lock release experiments were conducted to investigate the qualitative and quantitative properties of gravity current flow over sinusoidal topography in a two-layer ambient. Density differences between fluids are limited to a Boussinesq regime and are described by the density ratio, $S \equiv (\rho_1 - \rho_2)/(\rho_0 - \rho_2)$ where ρ_0 is the gravity current fluid density, ρ_1 is the lower ambient layer density, and ρ_2 is the upper ambient layer density. Bottom boundary topographic profiles are characterized by the ratio of amplitude to the average channel depth, A/H, and one-quarter the mean absolute slope, A/λ, where λ is the topographic wavelength. Initial fluid depths are described by the fractional lock-fluid height, D/H, and the fractional lower layer height, h_1/H. Particular emphasis is placed on analyzing the average slumping speed resulting from initial conditions, for which trends with S, D/H, h_1/H, A/λ are described along with the relative unimportance of A/H for $0.1 < A/H < 0.4$. Despite large A/H, the instantaneous front speed of the gravity current typically stays relatively constant as a result of the counterbalancing influences from contracting/expanding streamlines and along-slope variations in the buoyancy force. Qualitative properties such as interfacial motions

up- and downstream of the front and large Kelvin-Helmholtz vortices downstream of topographic peaks leading to sloshing motions are identified and described. Also identified is the early-time critical density ratio, S_{crit}, for which the interfacial disturbance created by the collapse and propagation of the lock-fluid transitions from travelling faster (subcritical gravity current) to slower (supercritical gravity current) than the average gravity current front speed. Finally, a model is presented that predicts the minimum number of topographic peaks the gravity current will overcome in the long time limit.

Preface

The work incorporated into Chapters 3 and 4 has been submitted for publication as M. Nicholson and M. R. Flynn, "Gravity current flow over sinusoidal topography in a two-layer ambient" to *Physics of Fluids*. I was responsible for carrying out all laboratory experiments, post-processing, and analysis of experimental images. Preliminary experiments of the type described in section 4.1 were conducted by Mr. Alan W. Tan in 2010 but were never published.

Acknowledgements

I would like to thank Dr. Morris Flynn for his patience, thoughtful guidance, and continuous wisdom through my time at the University of Alberta. To my family, friends, and especially my parents, thank you so much for all your support and encouragement.

Funding for this research was generously provided by the Natural Sciences and Engineering Research Council through the Discovery Grant and Research Tools and Instruments programs.

Contents

List of Tables

List of Figures

Chapter 1

Introduction and overview

A gravity current is a buoyancy-driven horizontal flow generated by a density difference between fluids. It is an important research topic because horizontal disparities in density can arise for a number of reasons in natural and industrial processes. A particularly dramatic example of a gravity current is a haboob or avalanche resulting from significant suspended particulate effectively increasing the surrounding air density and thus producing, respectively, horizontal and downslope flow. Other meteorological gravity currents generally form as a result of a temperature differences. A familiar example is that of a thunderstorm outflow, which arises when the air below a nimbus cloud is quickly cooled as a result of latent heat changes. Alternatively, a saline wedge in an estuary provides an example where differences of solute concentration result in gravity current flow. On a smaller scale, gravity currents often arise in industrial applications when two fluids of different densities are mixed together, for example, when tailings slurry is discharged into a containment pond. On the basis of these and other examples, it is fair to conclude that gravity currents are ubiquitous in nature and

industry which makes them relevant as a topic for study in connection with agriculture, nutrient transport in ecosystems, pollution dispersion, industrial processes, among others described in depth by Simpson (1997).

In the last three-quarters of a century, gravity currents forming between two uniform fluids and propagating over a flat horizontal boundary have been thoroughly examined in many notable studies. More specifically, and as described in further detail in Chapter 2, von Kármán (1940), Yih (1965), Benjamin (1968), Huppert & Simpson (1980), Rottman & Simpson (1983), Shin et al. (2004), and many others have comprehensively investigated and characterized gravity current flow with particular emphasis on analytically describing the front speed. Later on, Maxworthy et al. (2002), Ungarish (2006, 2009), Tan et al. (2011), White & Helfrich (2008, 2012), and others considered the same problem but with an ambient layer that is density-stratified in the vertical direction, z, a complication of direct relevance to oceanic and atmospheric flows. In fact, a density-stratified ambient is a factor for almost all large scale environmental flows due to phenomena such as atmospheric inversions and ocean thermoclines. Another complication that is almost always present for gravity currents that arise in natural settings is a bottom boundary that is rough, uneven, or undulating. In that regard, the effects of different bottom boundaries on gravity currents have been investigated by Nogueira et al. (2013) for rough beds and by Rottman et al. (1985), Lane-Serff et al. (1995), Özgökmen et al. (2004), Gonzalez-Juez et al. (2009), and Tokyay

et al. (2011, 2014) for bottom boundary obstacles and bedforms. However, with the exception of Özgökmen et al. (2004), all of these studies are restricted to an ambient layer that is of uniform density. The presence of ambient stratification can be influential to flow because it allows for the generation of internal waves. Ambient stratification becomes even more important when topographic height variations are of comparable vertical length-scale to the scale over which appreciable changes of density occur. This study aims to investigate experimentally a much less idealized scenario than previous foundational studies by combining a corrugated bottom boundary with a vertically stratified ambient on lock-release gravity current flows.

Due to the lack of previous study in this area and in an attempt to minimize the influence from separation effects brought about by sharp corners, the topography used herein has a smooth sinusoidal profile. The parameter space associated with such a topographic profile is described by the non-dimensional topographic amplitude, A/H, and one-quarter the mean absolute slope, A/λ where λ is the topography wavelength – see figure 3.1 below. Moreover, the non-dimensional topographic height is restricted to $0.1 < A/H < 0.4$ so as to avoid duplicating the results of either gravity current flow over rough beds in the lower end of the range (e.g. Nogueira et al., 2013) or flow up a slope in the higher end of the range (e.g. Marleau et al., 2014). To simplify comparisons with studies like Tan et al. (2011) and Sahuri et al. (2015), the ambient layer is restricted to a two-layer density profile comprising a lower layer of density ρ_1 and upper layer

of density ρ_2. In that regard, and also similar to the study of Tan et al. (2011), the ambient layer is described using the initial lower layer height normalized by the average channel depth, h_1/H and a density ratio, $S \equiv (\rho_1 - \rho_2)/(\rho_0 - \rho_2)$, where ρ_0 is the gravity current fluid density. The ambient lower layer height is varied so that the ambient interface is always above any topographic peaks, a restriction that, if violated, changes the nature of the problem in ways too complicated to explore here. Experiments are separated into two categories: full-depth lock release runs where the initial gravity current height, D, spans the entire channel depth and partial-depth lock release runs where the initial gravity current height is decreased so that $D/H = 0.5$ or $D/H = 0.75$.

In Chapter 2, §2.1 will provide a brief overview of contributions from early foundational studies that describe gravity current flow over a flat horizontal boundary; §2.2 will describe studies that have examined gravity current flow over topography; and §2.3 will provide a description of studies that have analyzed gravity current flow through a density-stratified ambient. Combining the scenarios of Chapter 2, Chapter 3 will outline the experimental setup and procedure used to examine rectilinear gravity current flow over sinusoidal topography in a two-layer ambient. Results are discussed in Chapter 4, which is separated into sections based on front speed (§4.1), motions up- and downstream of the gravity current front (§4.2), and the downstream distance travelled in the long time limit (§4.3). Finally, in Chapter 5, overall conclusions are stated and discussed along with ideas for future research.

Chapter 2

Literature review

2.1 Gravity currents in a uniform ambient

The simplest case of gravity current flow is a fluid of density ρ_0 flowing into a fluid of density ρ_1 over a horizontal boundary where $\rho_0 > \rho_1$. When studying gravity currents experimentally, arguably the most important quantity to measure is the gravity current front speed, U, the non-dimensional analog of which is the Froude number, Fr. A gravity current Froude number, Fr, is typically defined in one of two different ways: using the channel depth, H, as the vertical length scale, i.e. $\mathrm{Fr}_H = \frac{U}{\sqrt{g'H}}$, or using the gravity current height, h, as the vertical length scale, i.e. $\mathrm{Fr}_h = \frac{U}{\sqrt{g'h}}$. In either formula, $g' \equiv g\frac{(\rho_1-\rho_0)}{\rho_1}$ is the reduced gravity.

Analytically, it is useful to assume an inviscid flow where the Reynolds number, $\mathrm{Re} \equiv UH/\nu$, is large where ν is the kinematic viscosity. In one of the earliest studies on this topic, von Kármán (1940) analyzed the simple energy conserving steady state case of dense fluid flowing into a ambient of infinite depth ($H \to \infty$). Using a reference frame fixed on the gravity current front, von Kármán ap-

plied Bernoulli's equation along streamlines to find that $\mathrm{Fr}_h \simeq \sqrt{2}$, assuming irrotational horizontal ambient flow outside and no relative flow inside the gravity current. Similarly, Yih (1965) used energy arguments to show that a simple rectangular gravity current which occupies half the channel depth ($h = \frac{H}{2}$) will have $\mathrm{Fr}_H = \frac{1}{2}$ or equivalently $\mathrm{Fr}_h = \frac{1}{\sqrt{2}}$. Later, Benjamin (1968) produced a seminal analysis when he criticised von Kármán's approach based on its failure to balance momentum fluxes in the flow. Benjamin then simultaneously reproduced the von Kármán (1940) result and came up with an expression that bridged the gap to Yih's result by using reasoning based on conservation of horizontal momentum. Benjamin's result assumes hydrostatic conditions far up- and downstream and relates Fr to the height of the gravity current and the channel depth, i.e.

$$\mathrm{Fr}_H = \sqrt{\frac{h(H-h)(2H-h)}{H^2(H+h)}}, \quad \text{for } 0 < h \leq \frac{H}{2} \tag{2.1}$$

In a much more recent study, Shin et al. (2004) argue that, contrary to the conclusions of Benjamin (1968), dissipation is unimportant for high Reynolds number flows. Their hydraulic analysis uses a control volume that encompasses both the ambient and the lock region which allows for the transfer of energy from behind the current, unlike the moving frame analyses of von Kármán, Yih (1965), and Benjamin (1968). Shin et al. (2004) find that a gravity current in a deep channel will have $\mathrm{Fr}_h = 1$ instead of the previous $\mathrm{Fr}_h = \sqrt{2}$ result. However, critics of the Shin et al. (2004) method (e.g. Ungarish, 2009) believe that their assumption of a rectangular shaped

gravity current is a significant oversimiplification that renders the model invalid, despite good agreement with laboratory experiments. A more philosophical criticism has to do with the initial condition that gives rise to the flow. In the analysis of Shin et al. (2004), knowledge of this initial condition is necessary in order to compute the front speed for $t > 0$. By contrast, Benjamin's analysis requires no such detailed information. Thus (2.1), which relates the front speed to the gravity current height just behind the front, makes no reference to the initial depth of gravity current fluid, D, relative to the channel depth, H.

The temporal evolution of the flow beyond the constant velocity slumping phase was first studied by Huppert & Simpson (1980) and Rottman & Simpson (1983) who found, through scaling analysis, that gravity currents propagating over a flat horizontal boundary in a uniform ambient evolve through three sequential flow regimes starting from $t = 0$: a slumping phase where the gravity current front or "nose", x_N propagates downstream at an approximately constant speed ($x_N \sim t$), a buoyancy-inertia phase where the self-similar gravity current decelerates according to a balance of inertial and buoyancy forces so that $x_N \sim t^{2/3}$, and finally, a buoyancy-viscosity phase where the gravity current is thin and therefore a balance of buoyancy and viscosity forces primarily control front speed and deceleration ($x_N \sim t^{1/5}$).

So far, all of the studies mentioned in this chapter only consider flow over a perfectly flat and horizontal surface, an idealization which rarely holds true for naturally occurring flows. When the

bottom boundary is not flat, it is no longer possible to apply self-similar scaling arguments confidently like the ones outlined above. For this reason, and because this study incorporates topography, emphasis is placed on the analysis of the gravity current slumping speed.

2.2 Gravity currents over topography

Fundamental studies of bidirectional flows over topography have been carried out by Armi (1986), Farmer & Armi (1986), Pawlak & Armi (2000), Smeed (2000), and others to describe how steady state exchange flow is influenced by topography. Farmer & Armi (1986) found that exchange flow over topography can occur in a number of different modes but that maximal two-layer exchange flow over a sill happens when the lower layer spans 3/8 of the height above the sill. This result can be applied to the study of the quasi-steady flow that occurs behind the gravity current head e.g. in predicting the gravity current height as it flows over topographic peaks (see §4.1), especially when the ambient layer is uniform.

Gravity currents influenced by drag have been studied extensively in the past few dozen years. Preliminary analytical models were developed by Hatcher et al. (2000) for a three-dimensional gravity current experiencing drag while propagating through an array of bed-mounted obstacles spanning the entire channel depth. Hatcher et al. (2000) show there exists the possibility of a self-similar buoyancy-turbulent drag regime (see their figure 8) following

the buoyancy-inertia flow regime that evolves as $x_N \sim t^{1/2}$. On the other hand, Hogg & Woods (2001) study a gravity current experiencing a bottom boundary drag due to flow over a rough surface and indicate a regime after the slumping phase for planar, constant flux gravity currents whereby $x_N \sim t^{4/5}$. In fact, because of the high aspect ratio undulating bottom boundary studied here, the same restrictions that limit the application of Huppert & Simpson's scaling analysis also apply for the analyses of Hatcher et al. (2000) and Hogg & Woods (2001).

Gonzalez-Juez & Meiburg (2009) investigate, by way of steady shallow-water theory in comparison with direct numerical simulations (DNS), how a two-dimensional gravity current is influenced by a single, rectangular obstacle. They describe the height and front speed of the gravity current as a function of the obstacle dimensions and upstream Froude number. In other studies that focus on the interaction of gravity currents with an uneven and periodic bottom boundary, Tokyay et al. (2011, 2014) used DNS to study large and small volume lock release gravity currents over an array of dunes and square ribs. They found that the duration of the slumping phase depends on the drag per streamwise length acting on the gravity current. In the high drag case, similar to the $x_N \sim t^{1/2}$ Hatcher et al. (2000) result, they discovered a buoyancy-drag regime but with the front position advancing as $x_N \sim t^{0.72}$. Tokyay et al. (2011, 2014) also comprehensively describe the qualitative flow features observed as a gravity current flows over an array of obstacles. Most notably, they describe a hydraulic jump that forms upstream of an

obstacle and a jet-like flow on the downstream side of the obstacle that evolves into a Kelvin-Helmholtz vortex. Tokyay et al. (2011, 2014) refer to such vortices as "intensive mixing vortices."

Özgökmen et al. (2004) even went so far as to study gravity currents flowing over topography in a stratified ambient. However, their study was motivated by the geophysical example of oceanic overflows. They therefore considered a bottom boundary that was undulated and on a declining slope. As a result, the gravity current transformed into an intrusion once its density matched that of the environment. Theirs is a problem similar, but not altogether comparable, to this study.

2.3 Gravity currents in a two layer ambient

When considering gravity current flow over topography, it is reasonable to expect changes in elevation to bring about non-negligible changes in ambient fluid density. Though a stratified ambient in conjunction with topography is a relatively unexplored topic (Ozgokmen et al. 2004 being a notable exception), gravity currents flowing through a vertically stratified ambient have been well investigated when the bottom boundary is horizontal. The effects of linear ambient stratification have been studied by Maxworthy et al. (2002) and Ungarish (2006, 2009) while two-layer stratification has been investigated by Tan et al. (2011). White & Helfrich (2008) even studied gravity currents propagating in a continuous non-linear density-stratification.

Most related to this study, Tan et al. (2011) developed a model to describe a gravity current flowing under a two-layer ambient using conservation of horizontal momentum and Bernoulli's equation in a similar fashion to Benjamin (1968). Tan et al.'s analysis allowed them to identify the parametric regime for which the interfacial disturbance generated by the collapse and propagation of the lock fluid travels faster than the gravity current front. A gravity current is deemed subcritical when it travels slower than the interfacial disturbance, critical if the speeds are approximately equal, and supercritical if the interfacial disturbance is propagating just in front of the gravity current head. They predict and verify using DNS and laboratory experiments that the transition from a subcritical to a supercritical gravity current flow occurs when $S\text{crit} \simeq 0.75$, independent of the height of the ambient interface. Another important discovery was the minimal influence of the interface thickness on the front speed; Tan et al. (2011) show that the interface can span vertical distances of between 10% to 100% of the channel depth with almost no change in measured values of Fr (see their figure 10).

Chapter 3

Experiments

3.1 Equipment and experimental procedure

Experiments were performed in a 225.0 cm long by 25.0 cm wide by 30.0 cm tall glass tank which was uniformly backlit using an Electric Vinyl light sheet. Topography was cut from blue closed-cell Styrofoam using a hot wire guided by sinusoidal wooden forms that were fabricated with the aid of a band-saw. In order to avoid the complications associated with securing foam topography to the bottom of the tank, the topography was instead inverted, levelled, and secured, with the help of steel weights and C-clamps, along the free surface. Experiments were therefore run upside-down relative to the schematic of figure 3.1. Such a change of orientation does not alter the fundamental dynamics of the flow provided that density contrasts are modest so that the system is Boussinesq. A system is Boussinesq if the density differences between fluids is approximately less than $\sim 10\%$ (Spiegel & Veronis, 1960), which is the case here. Given this equivalence, and to be consistent with the earlier discussion, results will be presented and described assuming

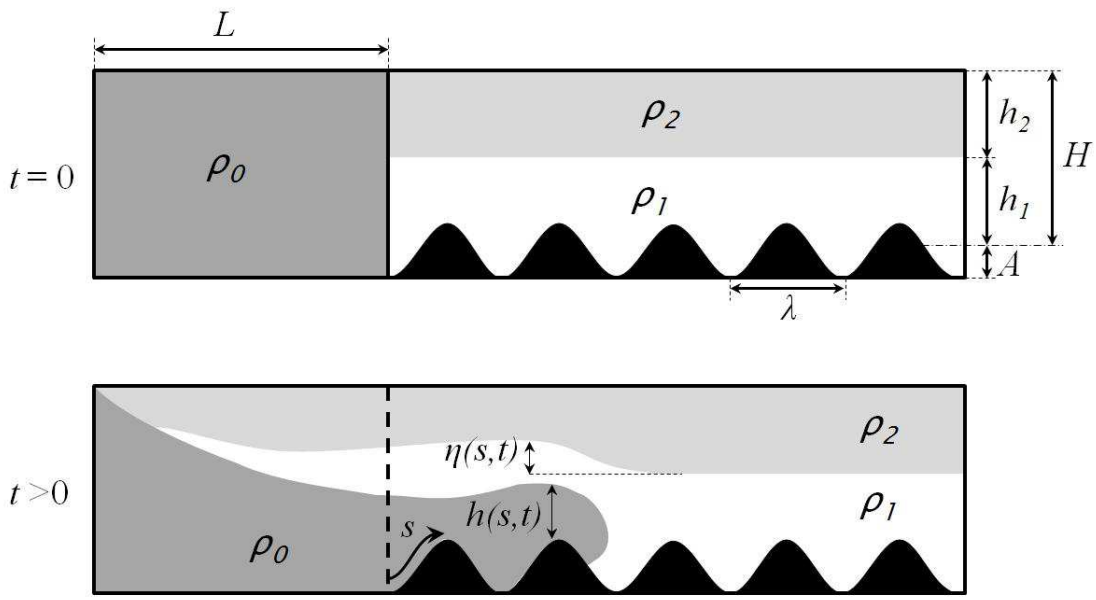

Figure 3.1: Schematic of a gravity current flowing over topography in a two-layer ambient.

a bottom-propagating gravity current as illustrated in figure 3.1. We can assume that the free surface, where it is present, acts as a rigid lid because the flow speeds within each experiment are much less than the free-surface gravity wave speed, $\sqrt{gH}$ (Baines, 1995).

To achieve the different densities required for each experiment, salt was mixed with fresh water and dye (food colouring) was added for flow visualization purposes. The density, ρ_0, of the lock fluid (dyed red) and the density, ρ_2, of the lower layer (dyed blue) were in all cases set to the approximate values of 0.998 g/mL and 1.055 g/mL, respectively. This left ρ_1, the density of the clear upper layer, to dictate the value of the density ratio, $S \equiv (\rho_1 - \rho_2)/(\rho_0 - \rho_2)$, which is used to characterize the density differences between the fluid layers. Densities were, in all cases, measured to within ± 0.00001 g/mL using an Anton Paar DMA 4500 density meter.

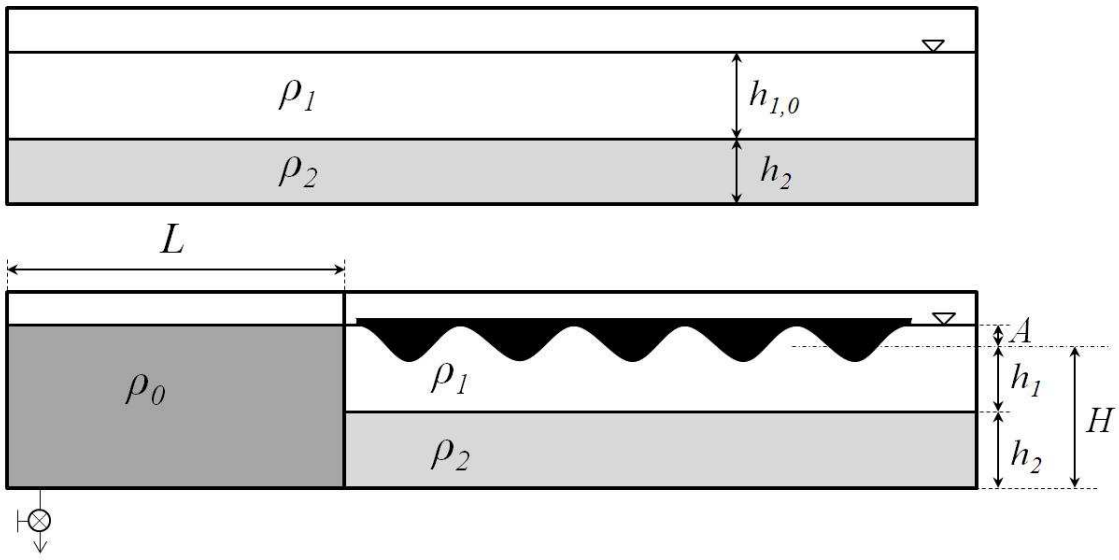

Figure 3.2: Schematic illustrating the tank filling process for a representative inverted full-depth lock release experiment. Note that $h_1 = h_{1,0} - A + V_{\text{sub}}/A_o$ where V_{sub} is the volume of the topography below the free surface and A_o is the plan area of the tank (including the lock and ambient regions).

The curvilinear coordinate, s, is chosen contrary to a simple horizontal coordinate, x, so that the speed of the gravity current reflects the total distance travelled over time. Measurements are converted from x to s using the formula for the arc length of a curve, i.e.

$$\mathrm{d}s = \sqrt{1 + \left(\frac{\mathrm{d}y}{\mathrm{d}x}\right)^2} \tag{3.1}$$

The variable y is the topographic height as a function of x position starting from the start of the topography, i.e.

$$y = -A\cos\left(\frac{2\pi}{\lambda}x\right) \tag{3.2}$$

The conversion from s to x is then

$$s = \int_0^x \sqrt{1 + \left(A\frac{2\pi}{\lambda} \sin\left(\frac{2\pi}{\lambda} x' \right) \right)^2} \, \mathrm{d}x' \tag{3.3}$$

3.1.1 Full-depth lock release experiments

To prepare the two-layer ambient, a layer of fresh water was first added to the tank to a depth of $h_{1,0}$. Granulated salt was then manually mixed into this fluid until its density reached a value of ρ_1. Once the salt was completely dissolved, residual turbulent motions were allowed to dissipate for 2 minutes before blue fluid of density ρ_2 was pumped underneath the clear layer using a Little Giant 3-MD centrifugal pump. In order to decrease the speed of the incoming fluid and to maintain well-mixed conditions in the reservoir containing fluid of density ρ_2, most of the fluid discharged by the pump was recycled to the supply reservoir using a return line controlled by ball valves. Moreover, the dense blue fluid was pumped through a sponge diffuser located along the bottom of the tank which minimized mixing between the two ambient layers. What mixing did occur was characterized by measuring the thickness of the interface between the upper and lower layers using a MSCTI conductivity probe (Precision Measurement and Engineering) connected to a Velmex stepper motor and controlled using LabVIEW software. The interface thickness was typically less than 2.0 cm, whereas H, the average channel depth, ranged from 10.2 cm to 18.0 cm. In any event, figure 10 of Tan et al. (2011) suggests that the interface thickness has only a minor impact on the front speed, at least in the case

Table 3.1: Sinusoidal topographic profiles.

	A	λ	A/λ	A/H
Profile 1	2.0 cm	24.0 cm	0.083	0.11
Profile 2	4.0 cm	24.0 cm	0.167	0.25, 0.39
Profile 3	4.0 cm	48.0 cm	0.083	0.25, 0.39

of gravity current flow over a horizontal boundary (for more details on the interface thickness, see Appendix D). The height, h_1, of the top clear layer was defined as the vertical distance from the ambient interface to the mean elevation of topography – see figure 3.2. Note that h_1 was either equal to, three times, or one-third of h_2, the depth of the lower ambient layer.

The fresh water lock-region was created by closing the lock gate at a horizontal distance of $L = 48.7\,\text{cm}$ from the left side of the tank and cycling in fresh tap water from above while simultaneously draining progressively more diluted lock fluid from a through-wall fitting and valve located on the bottom surface of the tank. Fresh water cycling occurred over a period of 15 minutes after which the valve was closed and the lock fluid was dyed red by addition of 3 mL of red food colouring. In total, filling the tank using the above procedure took between 3 and 4 hours depending on the value of h_2. Three sinusoidal topographic profiles were used with the geometric parameters outlined in table 3.1.

The range of A/H is chosen because, for $A/H \lesssim 0.1$, the flow resembles a gravity current propagating over a (very) rough bed, c.f. Nogueira et al. (2013). Conversely, for $A/H \gtrsim 0.4$, the flow resembles, locally, a gravity current propagating up or down a con-

stant slope, problems that have respectively been investigated by, for example, Marleau et al. (2014) and Bonnecaze & Lister (1999).

3.1.2 Partial-depth lock release experiments

With the inclusion of D/H, the parameter space associated with varying all of the above variables becomes very large. For the experiments described in this subsection, therefore, we restrict attention to ambient interface heights described by $h_1/H = 0.5$. A full factorial batch of experiments was run to characterize the flow dynamics associated with varying not only the topography but also S (six values between 0 and 1) and D/H (three values i.e. 0.5, 0.75 and 1.0).

To create the fluid layers the tank was first filled with fresh water to a height of

$$h_{1,0} = \frac{H}{2} + A - \frac{V_{\text{sub}}}{A_c} \tag{3.4}$$

where A_c is the planar area of the ambient region of the tank and V_{sub} is the volume of the topography below the free surface. Next, the lock gate was closed and salt was mixed into the ambient-side fluid until the target density of ρ_1 was achieved. Fresh water and approximately 3 mL of red dye were then added to the lock-region to a height of $h_0 = D + A$.

A ~ 50 L batch of blue dyed fluid having a density of $\rho_2 = 1.055$ g/mL was then mixed in a separate container. Using the same setup as described in §3.1.1, this blue dyed fluid was added very slowly outside of the lock to create a sharp interface between the upper and lower ambient layers. Once the free surface outside of

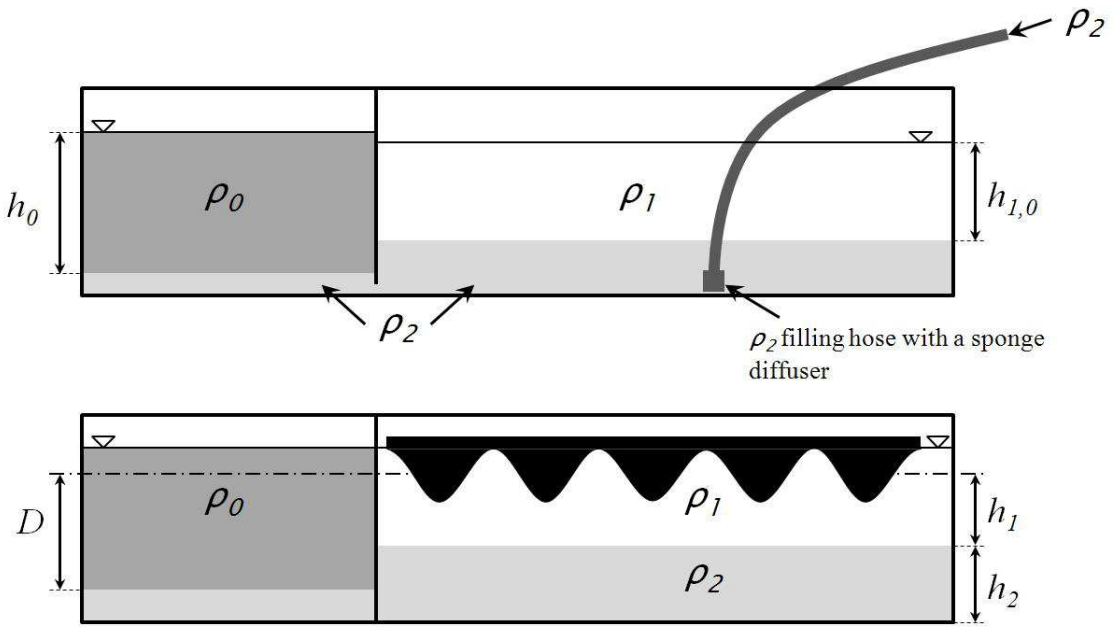

Figure 3.3: Schematic illustrating the filling process for a representative inverted partial-depth lock release experiment.

the lock was approximately 1 cm above the free surface inside of the lock, the hose was moved to the lock-side of the gate. Fluid addition continued until the lock fluid depth exceeded the ambient fluid depth by an amount $h_0 - h_{1,0} - \frac{1}{\rho_2}(h_0\rho_0 - h_{1,0}\rho_1)$. At this point, the two sides were approximately hydrostatically balanced and the lock-gate was opened very slightly to introduce a 0.3 cm gap along the base of the channel – see the upper panel of figure 3.3. The tank was then filled with blue fluid of density ρ_2 to a terminal depth of $H + A - V_{\text{sub}}/A_c$. Finally, the topography was very slowly lowered into the ambient-side of the tank and secured at the free surface with the gate still slightly open.

The lower panel of figure 3.3 shows the experimental initial conditions once the gate was subsequently closed. During this approx-

imately 3 hour filing process, the values of h_0, $h_{1,0}$, and the free surface heights on both sides of the gate with and without the topography were recorded .

3.2 Recording and post-processing of laboratory images

Experiments were recorded using a Canon Rebel EOS Rebel T3i camera. To minimize parallax errors, the camera was placed 3.75 m from the front of the tank. The CCD chip was located 1.35 m above the ground, coinciding with the approximate mid-depth of the channel. Note finally that the camera was positioned so that it pointed perpendicular to the middle of the topography. Experimental movies were trimmed, cropped, stripped of audio, and reduced from the default 24 fps variable frame rate to a 12 fps constant frame rate using Avidemux software.

All experimental images are analyzed "upside down" so as to be consistent with the orientation suggested in figure 3.1 and the discussion of Chapter 1. Correspondingly, the description of the experimental images and results will presume topographic elements placed along the bottom, not the top, of the channel. Post-processing of laboratory images was performed using a Matlab algorithm that exploited changes of pixel intensity to determine the gravity current height, h, as a function of time, t, and curvilinear position, s, which is defined in figure 3.1. The algorithm was based on (3.1) and (3.2) from Shin et al. (2004) and determines the gravity current height

using the depth-averaged blue component pixel intensity, devoid of subjective input on the part of the experimenter. Restricting attention to the blue component allowed the algorithm to interpret the two ambient layers as a single uniform layer. Thus for each column of pixels falling between the far left- and right-hand sides of the topography, the algorithm evaluated the depth-averaged gravity current height, h, or its nondimensional analogue, h/H. For each movie frame, therefore, the algorithm computed h/H in horizontal increments of approximately 0.11 cm between $x = 0.0\,\text{cm}$ and $x = 119.0\,\text{cm}$ for $\lambda = 24.0\,\text{cm}$ and between $x = 0.0\,\text{cm}$ and $x = 95.8\,\text{cm}$ for $\lambda = 48.0\,\text{cm}$. Finally, by combining data from all frames, composite time-series (CTS) figures showing h/H as a function of t^* and s/L were constructed (see figure 3.4 below). These are different from simple horizontal time-series because there is additional vertical time-series data incorporated into the plot using a colourbar. Here L is the lock-length and t^*, which is zero the moment the gravity current reaches the first trough of the topography, is defined as

$$t^* \equiv \frac{t}{H}\sqrt{g'_{02}H} \tag{3.5}$$

where g'_{02} is the reduced gravity of the system defined by,

$$g'_{02} \equiv g\frac{|\rho_0 - \rho_2|}{\rho_0} \tag{3.6}$$

Examples of three different vertical time-series (VTS) are shown in the bottom of figure 3.4; above these is the corresponding CTS

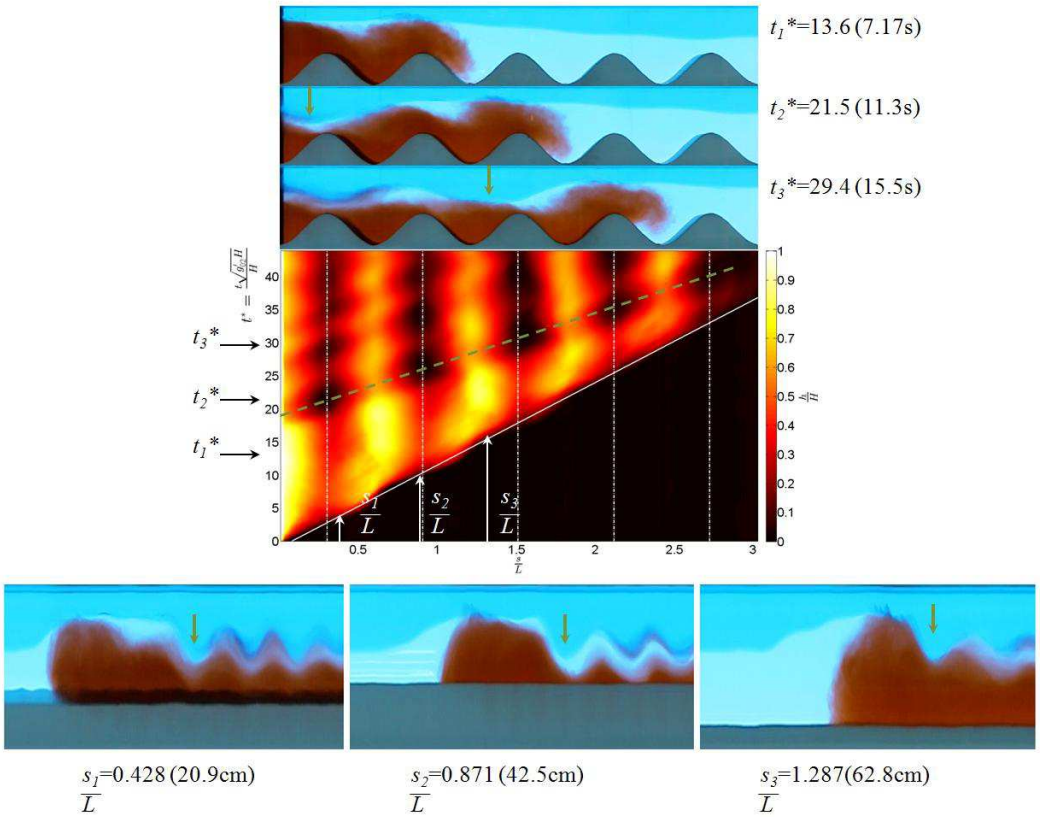

Figure 3.4: [Colour] Above, three snapshots of an experiment are shown at times $t_1^* = 13.6$, $t_2^* = 21.5$, and $t_3^* = 29.4$. These snapshot images have horizontal and vertical axis limits of $0.0\,\text{cm} \leq x \leq 119.0\,\text{cm}$ and $0.0\,\text{cm} \leq z \leq 22.2\,\text{cm}$, respectively, and are aligned with the composite time-series (CTS) shown in the middle where vertical dashed lines indicate the curvilinear location of the topographic peaks. The times t_1^*, t_2^*, and t_3^* are indicated by the black horizontal arrows. Below, three vertical time-series (VTS) that have horizontal and vertical axis limits of $0.0\,\text{s} \leq t \leq 23.3\,\text{s}$ and $0.0\,\text{cm} \leq z \leq 22.2\,\text{cm}$, respectively, and are shown at curvilinear positions $s_1/L = 0.428$, $s_2/L = 0.871$, and $s_3/L = 1.287$. These locations are indicated by the white vertical arrows. The green arrows and green dashed line indicate the position of the ambient reflected wave. Below the green dashed line is a diagonal white line whose slope specifies $\bar{U}$, the average initial front speed. Note that the dark band just above the topography in the left-hand VTS is a result of parallax where the far side of the topography is visible to the camera. Experimental parameters are as follows: $S = 0.732$, $D/H = 1.0$, $A/H = 0.242$, $A/\lambda = 0.167$, and $h_1/H = 0.509$.

image. The gravity current appears to be orientated "backwards" in the VTS because, with t being the horizontal axis variable, no gravity current fluid reaches the prescribed column of pixels until a certain time, dependent on the downstream location of the column of pixels relative to the lock gate, has elapsed.

From each CTS, the gravity current front position could easily be located. It was therefore possible to estimate a Froude number, $\mathrm{Fr} = \bar{U}/\sqrt{g'_{02}H}$, based on $\bar{U}$, the average initial front speed, which was found from the slope of the best fit line applied to those CTS data giving the (curvilinear) position of the front vs. t. When $\lambda = 24.0\,\mathrm{cm}$, the CTS data in question fell between the first and the third topographic peaks, except when the front did not propagate all the way to the third peak. In this case, and also when $\lambda = 48.0\,\mathrm{cm}$, the CTS data in question fell between peaks one and two. These intervals were specially selected to include up- and downslope segments of equal length and also guaranteed that the gravity current remained in the slumping phase, regardless of the experimental parameters.

The forward advance of the gravity current resulted in an ambient return flow in the form of a gravity current of fluid of density ρ_2 that flowed into the lock. When this gravity current reached the lock end-wall, it was reflected as an ambient reflected wave, which propagated downstream at a speed faster than $\bar{U}$. Figure 3.4 shows the position of the first trough of this ambient reflected wave with the green vertical arrows; these appear in both the snapshot and the VTS images. The curvilinear position of the first trough of

the ambient reflected wave is indicated in the CTS by the green dashed line. In the case of figure 3.4, and all the experiments described hereafter, the ambient reflected wave did not directly impact the reported Froude number because the wave did not overtake the gravity current front within the bounds in which Fr was measured. Nonetheless, it was possible to estimate whether the gravity current represented a supercritical or subcritical flow based on a comparison between the front speed and the speed of the interfacial disturbance excited by the forward advance of the gravity current. To estimate the interfacial disturbance speed, we first constructed CTS images showing the normalized displacement, η/H, of the ambient interface – see figure 3.5. The light band that runs from the bottom left to top right corresponds to the interfacial disturbance that lay above the gravity current head. Because the speed of this interfacial disturbance was larger than that of the front, the gravity current shown in figures 3.4 and 3.5 was of subcritical type. After the light band in figure 3.5 is a dark-coloured band that corresponds to the first trough of the ambient reflected wave and which appears when $t^* \simeq 18$ as anticipated by the green dashed line of figure 3.4. (Further discussion of sub- vs. supercritical flow is provided in §3.2 below.)

CTS images such as figure 3.5 are valuable because they also reveal vertical deflections to the ambient interface well ahead of the gravity current front. Attention is here focused on the region below and to the right of the light band where a "checkerboard" pattern having wavelength λ can be seen. As confirmed by figure 3.5 and,

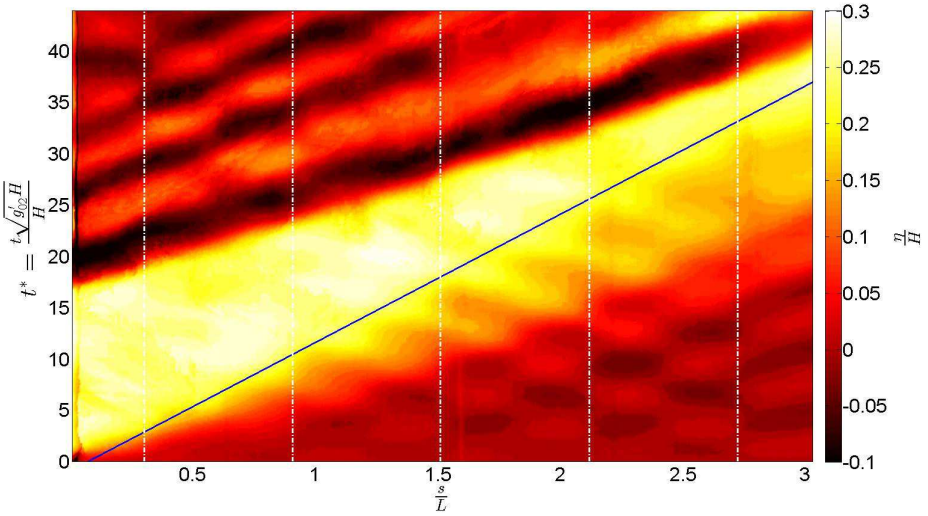

Figure 3.5: [Colour] CTS showing η/H for the same experiment as figure 3.4. The solid line is extracted from figure 3.4 and shows the average position of the gravity current front. Ahead (bottom right side of the solid line) and behind (top left side of the solid line) the front, interfacial motions are plainly evident. The bright band corresponds to the interfacial disturbance and the dark bands behind the front correspond to the first, second, third and fourth troughs of the ambient reflected wave.

more especially, figure 3.6, these downstream disturbances are of comparatively small amplitude. They arise because the bottom boundary is corrugated. Consequently the ambient return flow is spatially-variable rather than uniform.

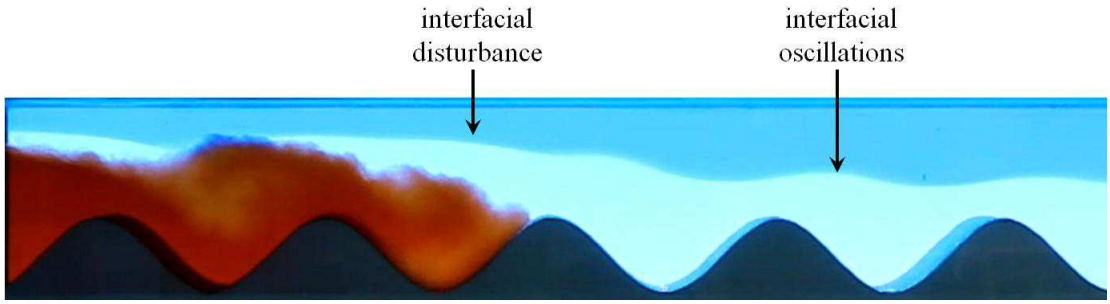

Figure 3.6: [Colour] Experimental snapshot at $t^* = 13.3$ showing an interfacial disturbance, which is due to the forward advance of the gravity current, and downstream oscillations, which are due to spatial variations in the ambient return flow. The ambient reflected wave is not yet visible. The above frame measures 115 cm long by 20.7 cm tall and experimental parameters are as follows: $S = 0.534$, $D/H = 1.0$, $A/\lambda = 0.167$, $A/H = 0.242$, and $h_1/H = 0.504$.

Chapter 4

Results

4.1 Gravity current front speed (for full- and partial-depth lock release gravity currents)

Figure 4.1 shows Fr for the full-depth lock release gravity currents vs. the density ratio, S, for different values of h_1/H, A/H, and A/λ. The data from figure 4.1 consist of 30 two-layer, flat-bottom experiments from the work of Tan et al. (2011) combined with 54 two-layer experiments with topography included. Note that figure 4.1 a with $h_1/H \simeq 0.25$ contains fewer data points than does figure 4.1 c with $h_1/H \simeq 0.75$ because of the requirement that the ambient interface must lie strictly above the topographic peaks.

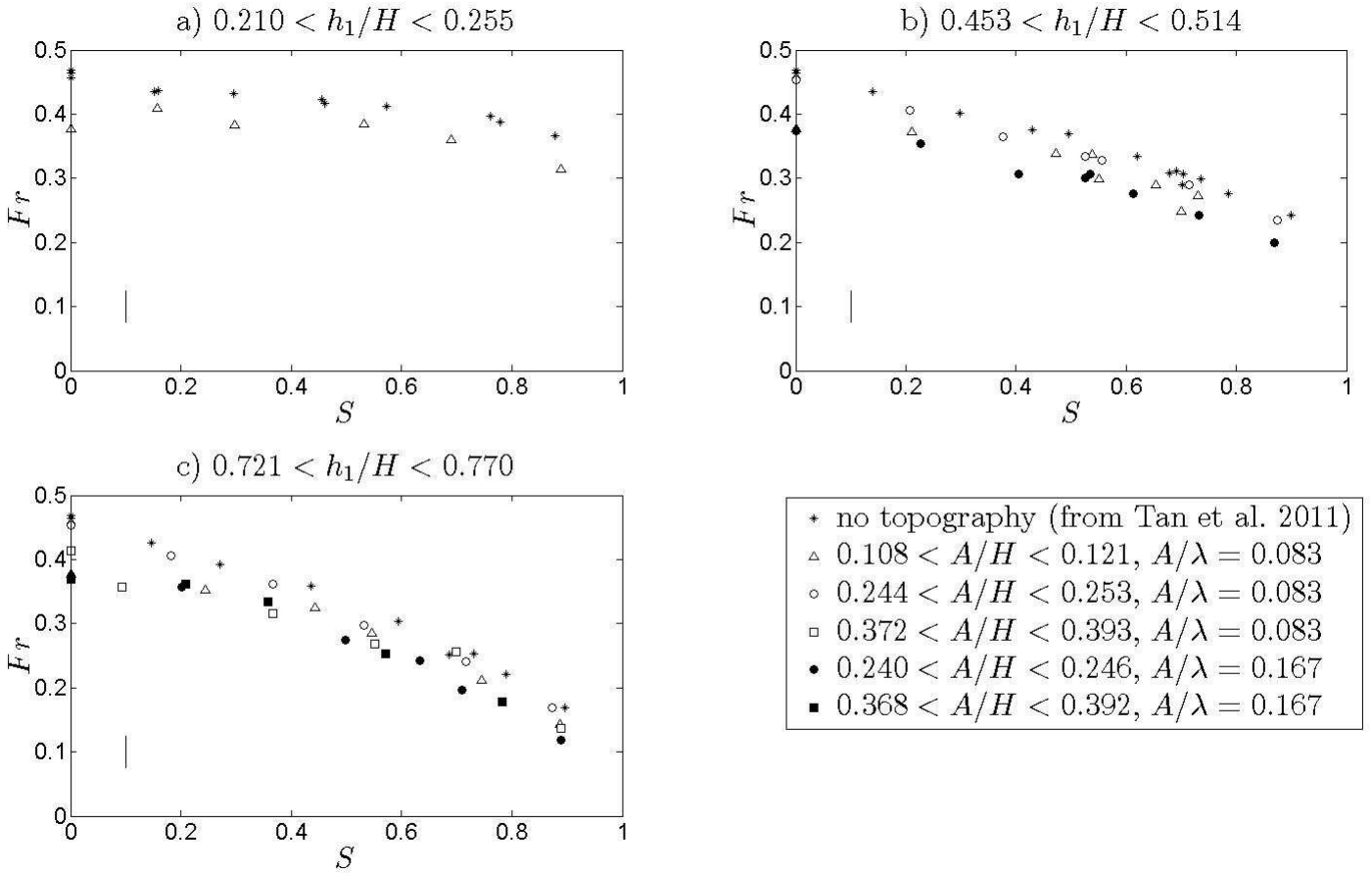

Figure 4.1: Variation of Fr with S for $D/H = 1$ various h_1/H, A/H and A/λ. Representative error bars based on the results of repeat experiments are as indicated in the bottom-left corner of each panel. Error bars in the horizontal direction are comparable to the width of the vertical error bar.

For both experimental data sets, Fr decreases as S increases. This behavior becomes more pronounced for larger h_1/H: as the lower layer depth increases, the depth-weighted mean density decreases and the driving force for motion (which depends on the difference of density between the gravity current and the ambient) diminishes. The forcing imparted by the topography also acts to decrease Fr. Note, however, that data points having the same value of A/λ cluster to a greater extent than do data points with the same value of A/H, even for A/H as large as 0.4. In other words, for the undulating topography of interest here, it is the topographic slope rather than the topographic amplitude that plays the more substantial role in setting the front speed. This assertion is confirmed by figure 4.2; it indicates that Fr changes very little as a function of A/H when all other experimental parameters are held constant. Consistent with the above statement, Tokyay et al. (2011) suggest that the form drag of a bottom surface obstacle depends on its "degree of bluntness" which, for the sinusoidal topography of interest here, is encapsulated by A/λ. In comparison, Tokyay et al.'s numerical simulation of a gravity current flowing over smooth dunes with $S = 0$, $A/H = 0.15$, and $A/\lambda = 0.05$ achieved $\mathrm{Fr} = 0.4$. Having a small A/λ, we would expect this result to be very close to the $S = 0$ flat bottom case ($\mathrm{Fr} = 0.46$) denoted by the starred data marker in figure 4.1. The discrepancy can partly be attributed to the non symmetrical dune shape which results in flow separation as the gravity current propagates over the topographic peaks, something that lowers the Fr but which, by design, is less of a factor

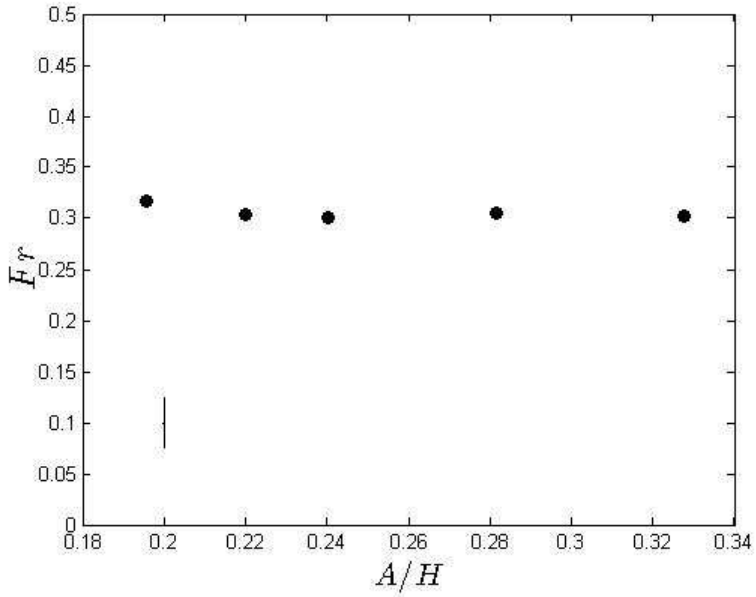

Figure 4.2: Variation of Fr with A/H for fixed values of A/λ ($A/\lambda = 0.167$), h_1/H ($0.49 < h_1/H < 0.51$) and S ($0.51 < S < 0.53$). A representative error bar based on the results of repeat experiments is indicated in the bottom-left corner of the figure.

for our sinusoidal topography. Tokyay et al. (2011) also report a Fr = 0.34 for square ribs with $S = 0$, $A/H = 0.15$, and $A/\lambda = 0.05$, which leads to the generic qualitative observation that both the shape of the bedform and its A/λ have a significant influence on the front speed of the gravity current.

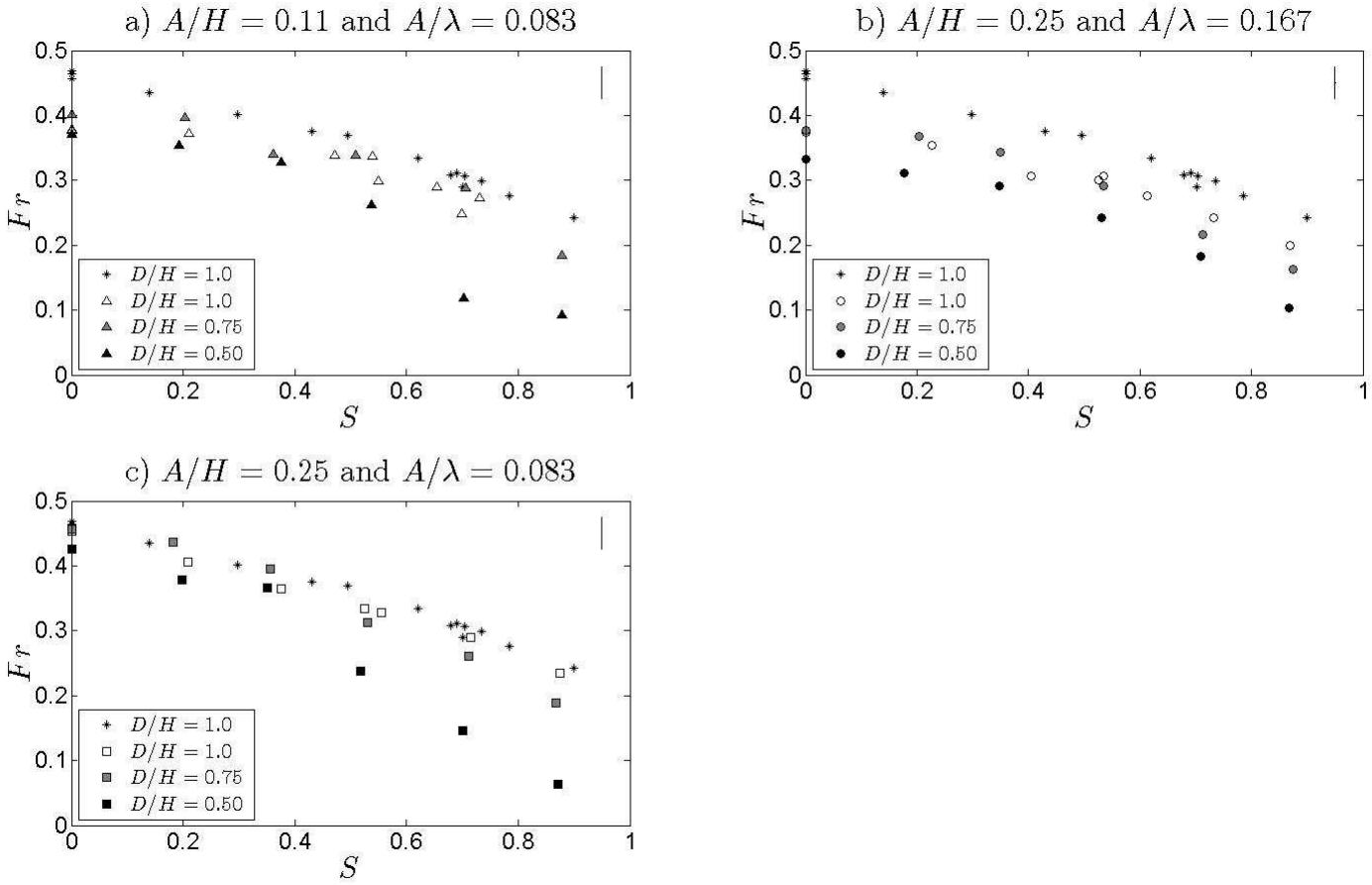

Figure 4.3: Variation of Fr with S for $h_1/H \simeq 0.50$ and various A/H, A/λ, and D/H. Representative error bars based on the results of repeat experiments are as indicated in the top-right corner of each panel. Error bars in the horizontal direction are comparable to the width of the vertical error bar. The starred $D/H = 1.0$ data shown above correspond to cases without topography and are drawn from the study of Tan et al. (2011).

Similar results to figure 4.1 are observed in the case of our 36 partial-depth lock release experiments. In particular, figure 4.3 presents data having various D/H but fixed ambient interface height, i.e. $h_1/H = 0.5$. More specifically, the figure shows the variation of Fr with S for three different topographic profiles. In contrast to figure 4.1 where data is divided into panels based on h_1/H, figure 4.3 separates data based on topographic profile in order to isolate the effect of changing D/H. For reference purposes we also include in figure 4.3 data from 15 full-depth lock release experiments drawn from the study of Tan et al. (2011) where no topography is present. Changing D/H does not alter the qualitative relationship between Fr and S: as with the data sets of figure 4.1, those of figure 4.3 indicate that Fr and S are inversely related whether D/H is comparatively large or small. Note, however, that when topography is present, the $D/H = 1.0$ and $D/H = 0.75$ data sets are almost indistinguishable, particularly for small and moderate S, whereas the $D/H = 0.5$ data shows a consistently smaller value for the front speed. Insights into this observation are obtained from figure 4.4, which shows, for different S and D/H, time-series of the gravity current height measured at the location of the first topographic peak. In all three panels, the height of the gravity current head is comparable for $D/H = 1.0$ and $D/H = 0.75$. When $D/H = 0.5$, by contrast, the head height is notably reduced suggesting a diminished driving force. The top panel of figure 4.4 indicates the maximal two-layer exchange flow solution, $h = \frac{3}{8}(H - A)$, derived by Farmer & Armi (1986). Farmer & Armi's theory presumes steady

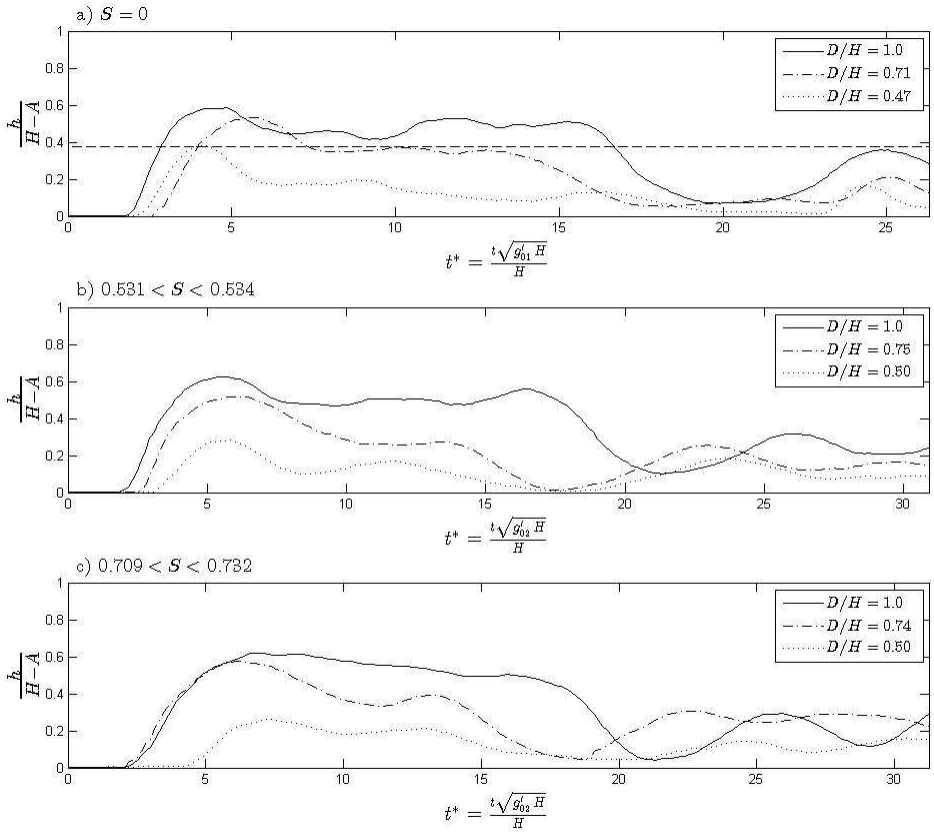

Figure 4.4: Gravity current height over the first topographic peak for three different values of S and D/H. The topographic profile is such that $0.234 < A/H < 0.246$ and $A/\lambda = 0.167$. The horizontal dashed line in panel (a) shows the steady two-layer exchange flow solution derived by Farmer & Armi (1986).

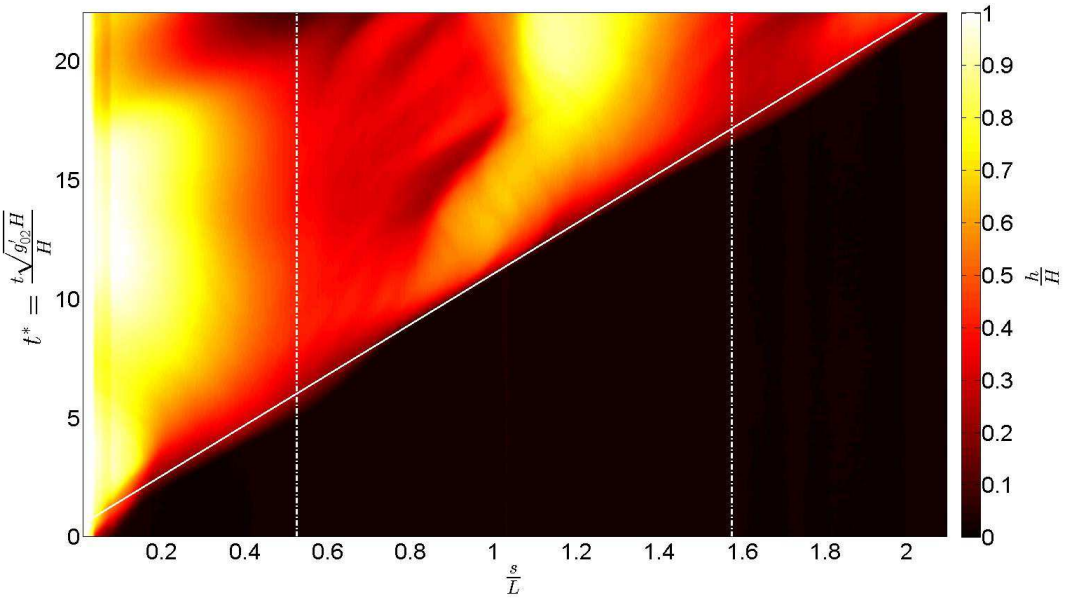

Figure 4.5: [Colour] CTS of an experiment where the gravity current front speed is nearly constant in spite of large variations in h/H. Experimental parameters are as follows: $S = 0.715$, $D/H = 1.0$, $A/\lambda = 0.083$, $A/H = 0.252$, and $h_1/H = 0.497$.

conditions and so is here applicable only if we examine the flow immediately behind the gravity current head. In this region, and allowing for the interfacial distortions caused by turbulent mixing, it seems likely that the exchange flow following the head is maximal when $D/H = 1.0$ and 0.75, but not when $D/H = 0.5$. Unfortunately, it is much more difficult to determine the maximal exchange flow conditions when the ambient is comprised of two layers, rather than just one. We do not, therefore, show horizontal dashed lines in the middle or bottom panels of figure 4.4 but instead refer the interested reader to Smeed (2000).

If the conclusion to be drawn from figures 4.3 and 4.4 is that a decrease of gravity current height results in a corresponding de-

crease in Fr, one might expect the front speed within a single experiment to vary as the front flows first up- then downslope over large amplitude topography. In fact, quite the opposite is true in most cases. A not dissimilar observation was made in the experimental study of Britter & Linden (1980) who examined downslope gravity current flow along an infinite slope. They noted that the front speed remained constant even as the gravity current head continued to increase in size due to entrainment and inflow from behind the head. Consider, for instance, figure 4.5 whose CTS shows substantial variations in h/H but only modest variations in Fr (similar behavior is noted in many other experiments, both those with $\lambda = 24.0\,\mathrm{cm}$ and $\lambda = 48.0\,\mathrm{cm}$). We believe that the reason for this unexpected observation is that the instantaneous front speed is influenced by the competing effects of channel expansion/contraction and by along-slope variations of the buoyancy force. In regards to the latter, note that the direction of the vertically-oriented buoyancy force varies relative to the surface tangent vector leading, in the absence of other factors, to upslope (downslope) deceleration (acceleration). On the other hand, channel expansion and contraction lead, in the absence of other factors, to an acceleration of the gravity current (and the ambient return flow) as the channel constricts (corresponding to upslope gravity current flow) and a deceleration as the channel expands (corresponding to downslope gravity current flow). A similar observation can be seen in steady state exchange flow over a sill, such as the Farmer & Armi (1986) case, where the Froude number of the lower layer goes from subcritical (Fr < 1)

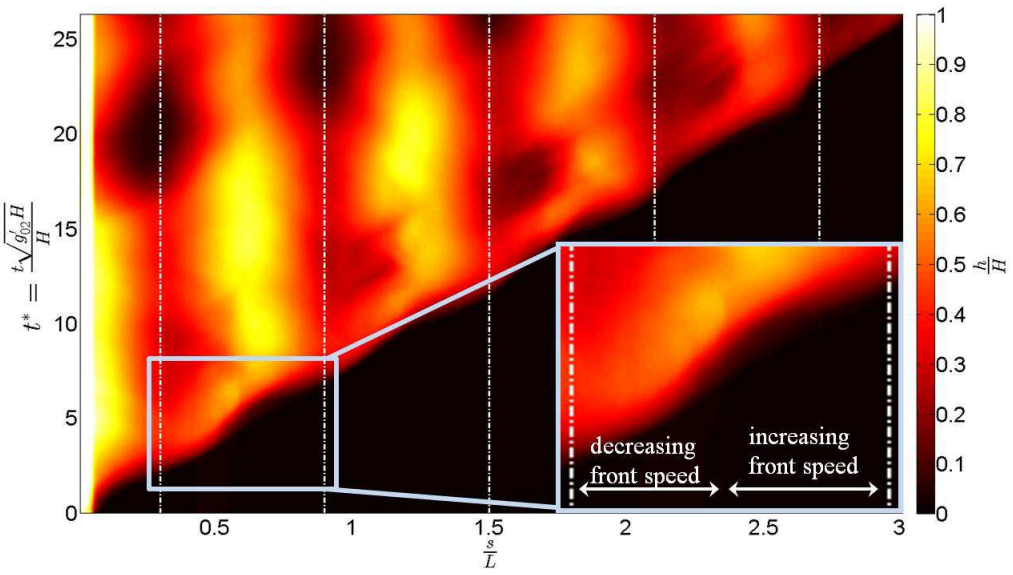

Figure 4.6: [Colour] CTS of an experiment where the gravity current front speed decreases (increases) on the downslope (upslope) portion of the topography. Experimental parameters are as follows: $S = 0$ (uniform density ambient), $D/H = 1.0$, $A/\lambda = 0.167$, $A/H = 0.246$.

before the topographic peak to critical (Fr = 1) at the topographic peak. Of course, the aforementioned influences cannot be expected to counterbalance in all circumstances. Indeed figure 4.6 shows a case where $S = 0$ corresponding to a uniform density ambient; here streamline expansion/contraction seems to play the more prominent role in modulating the advance of the front i.e. the front speed decreases on the downslope portion and increases on the upslope portion. As the inset to figure 4.6 makes clear, this deceleration and acceleration correspond, respectively, to convex and concave regions in the curve describing the temporal evolution of the front.

In still other circumstances, i.e. those where A/H is large, the ambient return flow appears to be important, as for example in figure 4.7, which shows an experiment where $A/H = 0.383$ and

the ambient fluid flowing opposite the gravity current exerts a non-negligible shear stress. The ambient return flow is here important for two reasons: *i*) the Reynolds number, $\mathrm{Re} \equiv \bar{U}H/\nu$ (where $\nu = 0.01\,\mathrm{cm/s^2}$ is the kinematic viscosity) is small, i.e. $\mathrm{Re} = 9,300$, compared to the average value of 13,800 for all full-depth lock-release experiments, and, *ii*) as the gravity current fluid nears the top of the first peak, partial blocking occurs resulting in only a thin overflow into the following trough. The gravity current is therefore of relatively modest volume flux and inertia. As a result, much of the gravity current fluid cannot ascend the second peak and so falls backwards into the first trough resulting in a sloshing-type motion of fluid of density ρ_0. Such sloshing behaviour is examined more thoroughly in the following subsection.

4.2 Motions upstream and downstream of the gravity current front

Sloshing motions behind the gravity current head were, in fact, relatively common in our experiments and were due to the formation of large Kelvin-Helmholtz vortices downstream of topographic peaks. This process is illustrated in figure 4.8, which shows a jet-like flow forming on the downslope portion of the first peak leading to a region of large shear – c.f. figure 2 of Gonzalez-Juez & Meiburg (2009). Consequently, and as anticipated by Pawlak & Armi (2000), a Kelvin-Helmholtz vortex starts to form on this downslope (or lee) side. The Kelvin-Helmholtz vortex demarcates the back of the

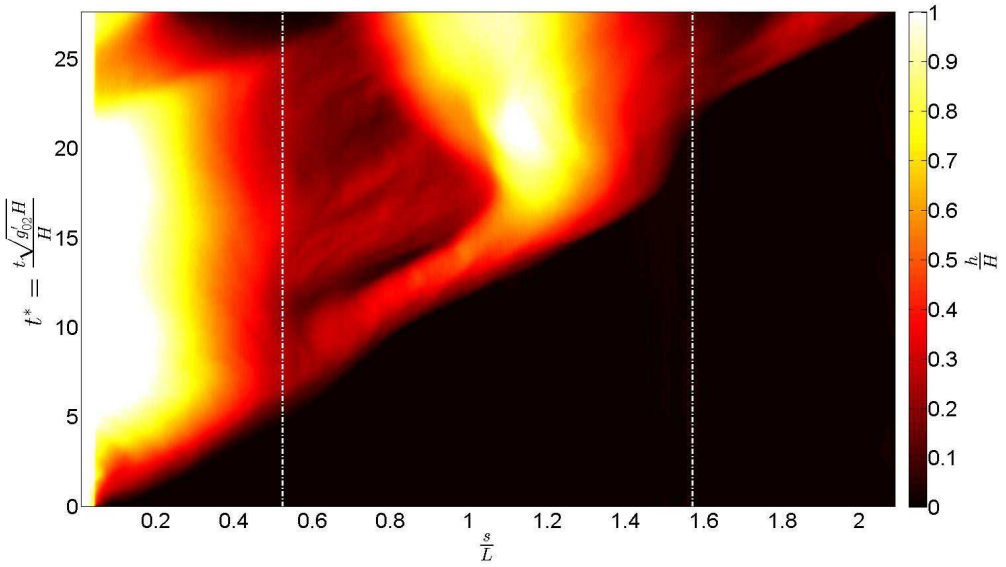

Figure 4.7: [Colour] CTS of an experiment where the gravity current nearly stops as a result of a strong ambient return flow at the second topographic peak. Experimental parameters are as follows: $S = 0.0938$, $D/H = 1.0$, $A/\lambda = 0.083$, $A/H = 0.383$, and $h_1/H = 0.750$.

gravity current head and is apparent as the front reaches the trough. When the front propagates up and over the second peak, the Kelvin-Helmholtz vortex, described by Tokyay et al. (2011) as an intensified mixing vortex, reaches a maximum diameter and downstream location. It then becomes unstable in the sense that dense gravity current fluid begins to flow backwards into the trough. Thus a sloshing mode is initiated, which in CTS images such as those of figures 4.8 and 4.9 is characterized by sideways-V-shaped light-coloured bands – see the circled areas in the latter figure. The lower branch of the V indicates the formation, growth, and saturation of the Kelvin-Helmholtz vortex and the upper branch indicates a relaxation process that leads to dense gravity current fluid settling midway between adjacent peaks. Loosely connected with these

transient events is the advection of gravity current fluid away from peaks by the ambient reflected wave. This results in peaks that are, sometimes temporarily, sometimes permanently, devoid of fluid of density ρ_0. The process just described is evident in figures 4.8 and 4.9 from the large dark regions centered on the vertical dashed lines for medium and/or large values of t^*.

The diameter, ℓ_0, of the largest Kelvin-Helmholtz vortex recorded in each experiment is normalized using D similar to the process used by Özgökmen & Fischer (2008). Typical ℓ_0/D values ranged from 0.1 to 0.84 and had a mean of approximately 0.44. To predict the diameter of a vortex like the one exhibited in figure 4.8, we sought a correlation between ℓ_0/D and the Richardson number, Ri, where

$$\mathrm{Ri} = g'_{10}\frac{0.4(H-A)}{(1.6\bar{U})^2} \tag{4.1}$$

Here $g'_{10} = g\frac{\rho_1-\rho_0}{\rho_0}$ is the reduced gravity based on the density difference between the gravity current and the lower ambient layer. The vertical length scale characterizing the mixing region, $0.4(H-A)$, is chosen based on empirical data from Borden & Meiburg (2013) applied to the smallest channel depth of the experiment. Finally, the velocity difference of $1.6\bar{U}$ is estimated using the theory of Farmer & Armi (1986) assuming uniform velocities within each layer. Unfortunately the above approach yielded results best described as mixed. In other words, and as can be confirmed from tables A.1 and B.1, the correlation between ℓ_0/D and Ri is less than definitive. This is not altogether surprising because Kelvin-Helmholtz vortex formation, growth and saturation are complicated processes influ-

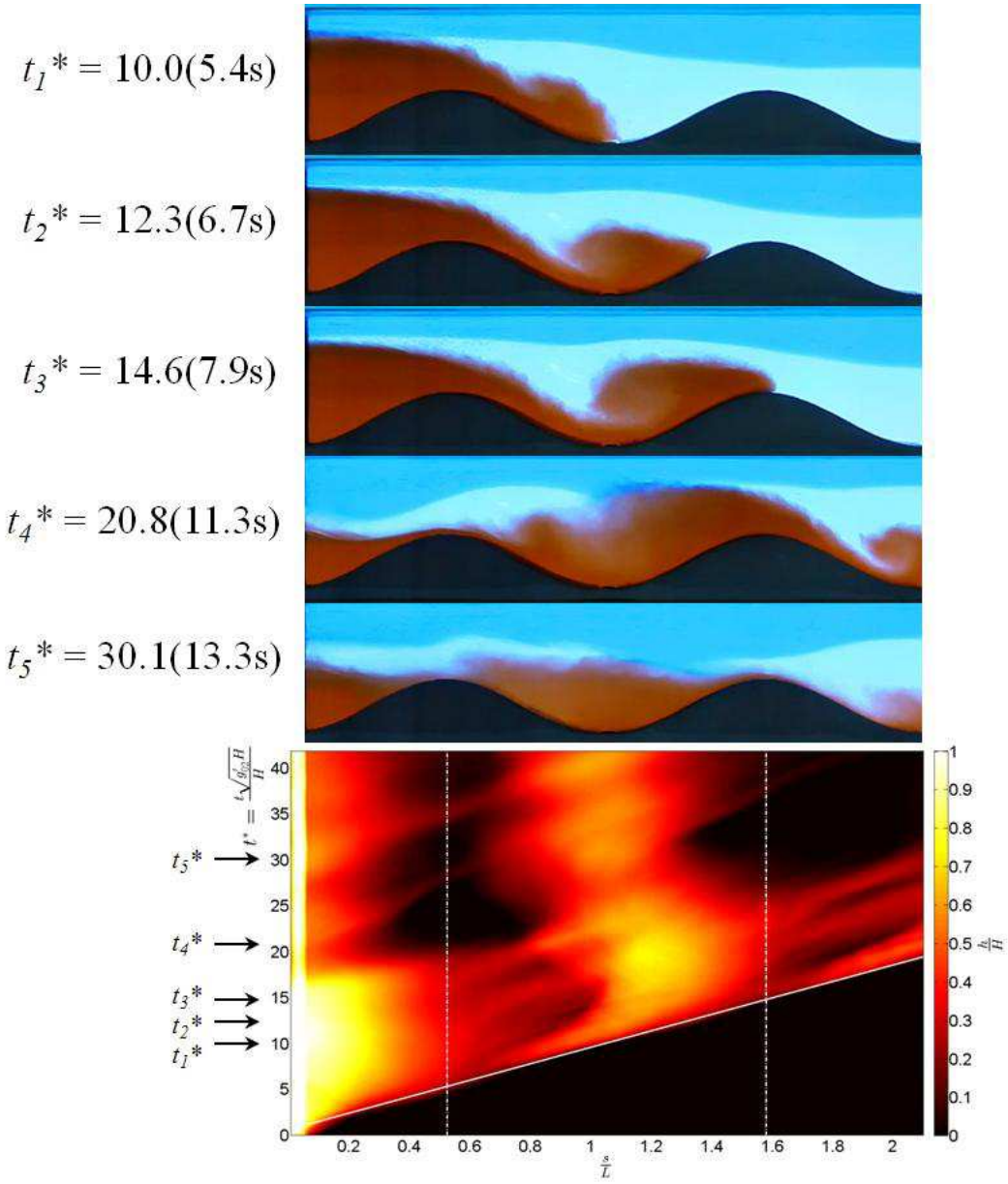

Figure 4.8: [Colour] Above: Experimental snapshots showing the development of a large-scale Kelvin-Helmholtz instability in the first trough. Below: the corresponding CTS. Experimental parameters are as follows: $S = 0.525$, $D/H = 1.0$, $A/\lambda = 0.083$, $A/H = 0.244$, and $h_1/H = 0.499$.

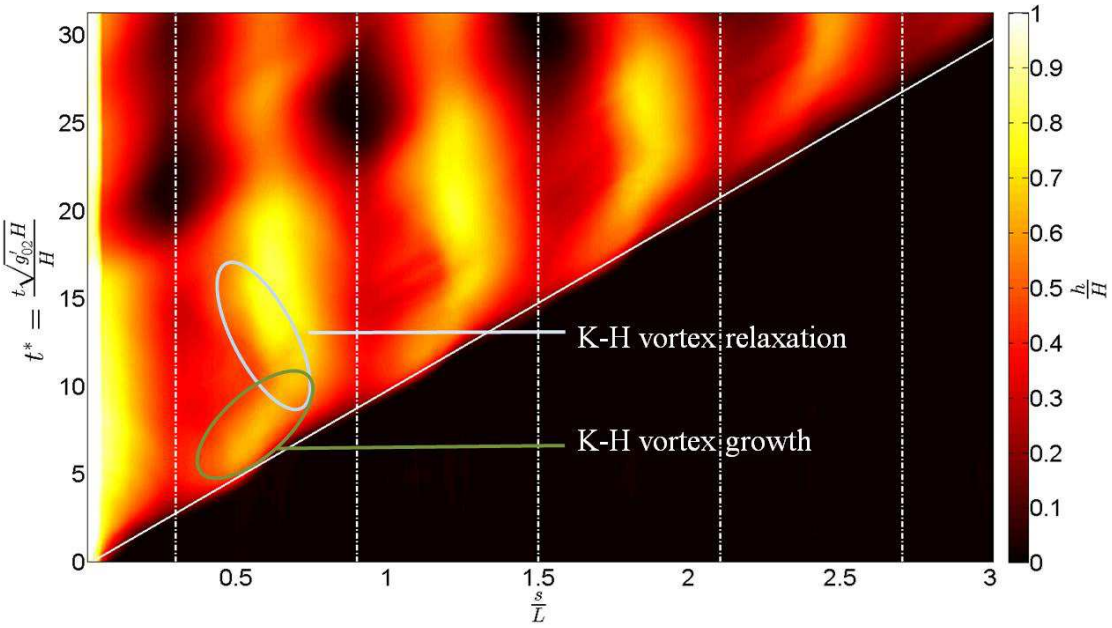

Figure 4.9: [Colour] CTS where gravity current fluid is initially skewed towards the downstream side of the first trough as a result of Kelvin-Helmholtz (K-H) vortex formation, growth, and saturation. As t^* increases, a relaxation occurs so that the light-coloured band settles into the middle of the trough creating a V-shape on the CTS. Experimental parameters are as follows: $S = 0.527$, $D/H = 1.0$, $A/\lambda = 0.167$, $A/H = 0.240$, and $h_1/H = 0.513$.

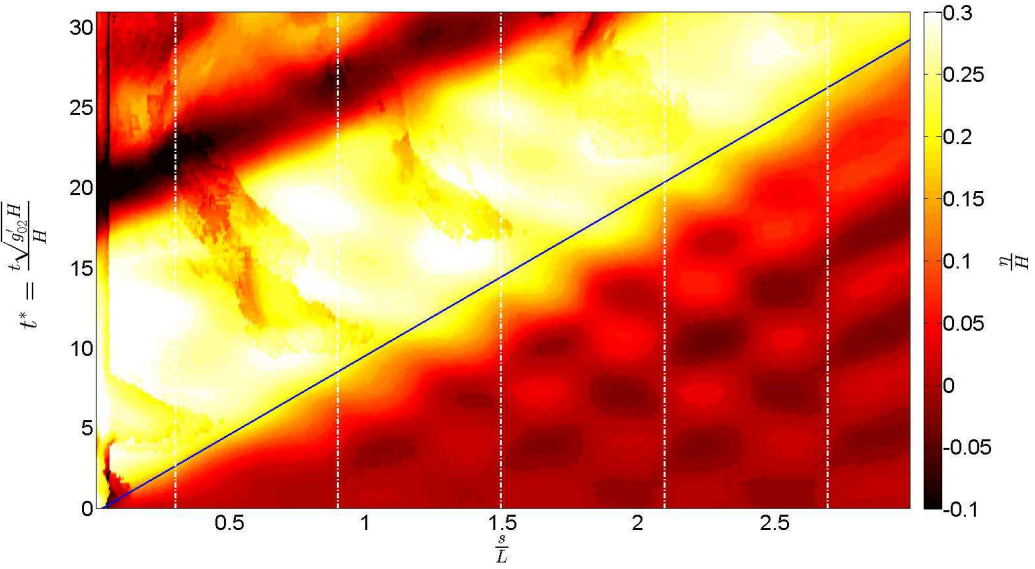

Figure 4.10: [Colour] CTS showing η/H for the same experiment as figure 3.6. The slope of the solid line indicates the average gravity current front speed. This can be compared against the speed of the interfacial disturbance, which can be recovered from the slope of the leading edge of the light band that starts in the lower left hand corner. Here these slopes are almost equal suggesting a gravity current that is nearly critical. Ahead of the front, interfacial oscillations are present– see also figure 3.5.

enced by numerous disparate factors. Although different definitions for Ri were attempted, including ones that incorporated the upper layer density, ρ_2, these proved no more helpful than the definition given by (4.1). Thus, it seems difficult to define a Richardson number that satisfactorily encapsulates the depths and densities of all three fluid layers, at least insofar as explicating the dynamics of unsteady vortices. Further investigation of this topic is therefore deferred to future studies.

A major focus of previous studies of gravity current flow through stratified media has been to identify parametric regime(s) where the front speed is greater than (supercritical flow) or less than (sub-

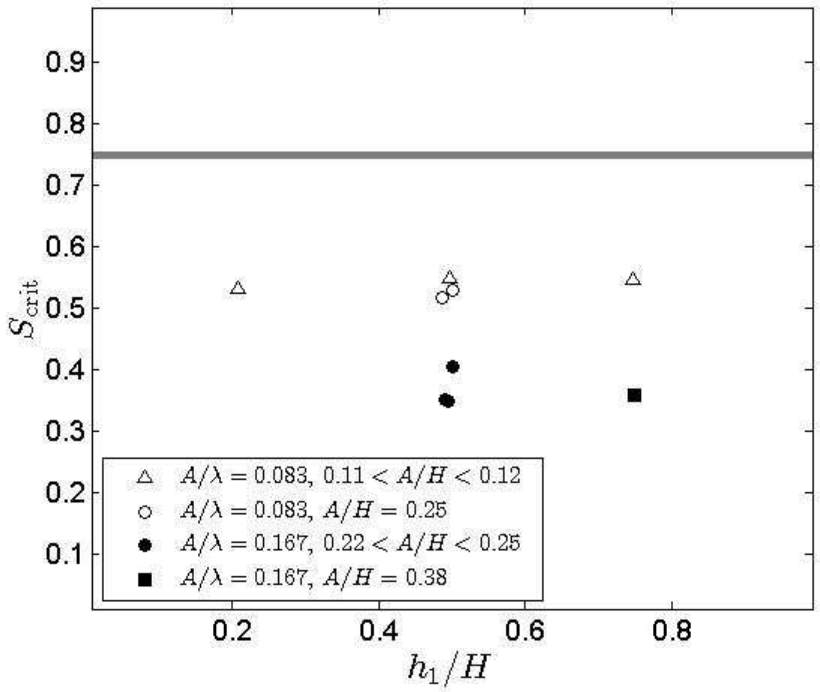

Figure 4.11: The maximum value of S where the gravity current flow is not subcritical plotted against h_1/H. The thick solid line indicates the prediction from Tan et al. (2011), which applies for a horizontal bottom boundary. Note that we did not attempt to collect data when $A/\lambda = 0.167$ and $h_1/H = 0.25$ because in this case the ambient interface would fall below the topographic peaks.

critical flow) the interfacial disturbance generated by the collapse and froward advance of the gravity current. For example, Tan et al. (2011) found that the transition from a super- to a subcritical gravity current occurred at approximately $S = 0.75$ independent of the ambient interface height, an observation in good agreement with analytical predictions. In the present context, the job of determining whether a particular gravity current is subcritical, critical, or supercritical is made easier, if not altogether easy, using CTS images of the types shown in figures 3.5 and 4.10. (The gravity current is respectively subcritical and approximately critical in the former and latter figures). Because critical and supercritical gravity currents can be difficult to distinguish, we seek, for fixed topographic profile and h_1/H, the largest value of S, S_{crit}, where the flow is no longer subcritical. Results are exhibited in figure 4.11, from which we conclude, consistent with Tan et al. (2011), that the interface height has a negligible influence. Thus $S_{\text{crit}} \simeq 0.75$ for $A/\lambda = 0$ (Tan et al. (2011)), $S_{\text{crit}} \simeq 0.53$ for $A/\lambda = 0.083$ and $S_{\text{crit}} \simeq 0.37$ for $A/\lambda = 0.167$. Similar to the front speed, A/H again seems to have a very small influence on the value S_{crit}.

One reason for distinguishing between sub- and critical/supercritical gravity currents above is that the latter generally travel further faster, which is particularly important when modelling the transport of potentially hazardous material in the natural environment. Here, the situation is made more complicated by the presence of topography because tall peaks can be more effective than interfacial disturbances at arresting the gravity current front – see figure

4.7, for instance. In subsection 4.3, we turn finally to the topic of the downstream distance travelled by the gravity current fluid.

4.3 Downstream distance travelled

One particular advantage of the partial-depth lock-release experiments is that the gravity currents have a comparatively modest volume and so do not always ascend all of the peaks comprising our topography. Thus we can compare the downstream distance travelled by the gravity current front in the long time limit with the minimum distance predicted by a simple geometric model in which gravity current fluid is supposed to fill the bottom of the tank to a vertical distance equal to the topographic height – see figure 4.12.

If mixing is neglected, the minimum number of peaks, $n_{\min}$, the gravity current fluid will overcome is given by

$$n_{\min} = \lfloor \frac{x_f}{\lambda} + \tfrac{1}{2} \rfloor \tag{4.2}$$

in which x_f, the horizontal distance defined in figure 4.12, is determined from

$$\left(\frac{D}{H} - \frac{A}{H}\right) L = 2a\frac{A}{H} + \int_0^{x_f} \left(\frac{A}{H}\cos\left(\frac{2\pi}{\lambda}x\right) + \frac{A}{H}\right) \mathrm{d}x \tag{4.3}$$

Here a is the distance from the lock-gate to the start of topography and L is the lock length. By construction, (4.2) and (4.3) are independent of S, the stratification parameter and h_1, the ambient interface height.

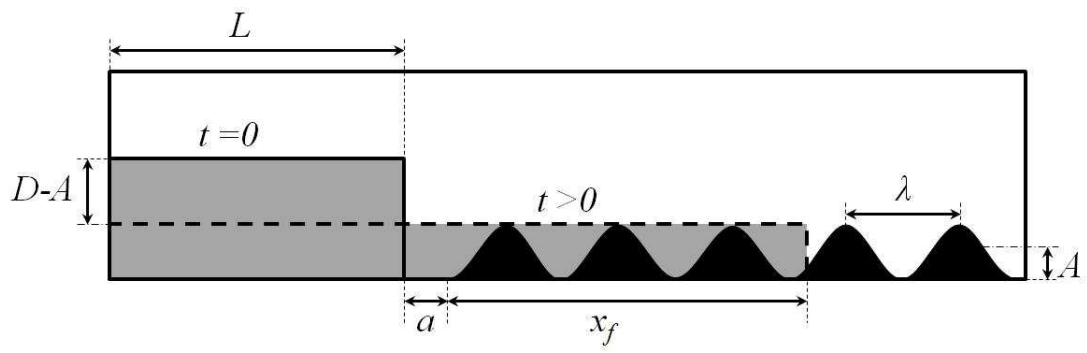

Figure 4.12: Schematic showing the minimum number of peaks overcome by a (partial-depth) lock-release gravity current. For simplicity, the ambient is here shown as having a uniform density.

In some instances, particularly those with large S, the downstream flow of gravity current fluid may be temporarily arrested well before the front reaches the ${n_{\min}}^{th}$ peak, however, dense fluid continues to overflow into each trough until its supply, determined by the product of D and L, is exhausted. The final number of peaks overcome in these experiments, plus those having small or moderate S, is specified in table 1. Each row of this table considers a family of experiments having a particular combination of A, λ, D and H but variable S in such a way that all full- and partial-depth experiments with $S > 0$ are represented in table 1. The fourth column specifies the prediction of (4.2) and (4.3) using $a = 0$. Corresponding experimental data are given in columns 5 and 6, which provide, respectively, measured values for $n_{\min}$ and $n_{\max}$. Also shown are the S values corresponding to these minimum and maximum values for n. For the first and second families of experiments (corresponding to the first seven rows of the table), the topographic profile has five peaks so we report "≥ 5" for those gravity currents that overcome

all five of these peaks. By contrast, there are only two peaks for the topographic profile in the third family of experiments (rows 8-11). Note that all partial-depth experiments have fixed h_1/H so we make no conclusions about the effect this ratio, which, in any event, does not appear in (4.2) and (4.3).

Of particular interest here are instances where the predicted value for $n_{\min}$ is less than the total number of peaks; $(n_{\min})_{\text{expt}}$ is greater than or equal to $n_{\min}$ in all such cases. When $(n_{\min})_{\text{expt}} = n_{\min}$, experiments generally exhibit minimal mixing and have a large S-value corresponding to a flow that propagates comparatively slowly downstream. Note, however, that the converse statement can be false, i.e. even when S is large, $(n_{\min})_{\text{expt}}$ may exceed $n_{\min}$ as is the case, for instance, in the large S case from row 5. In that experiment substantial mixing was observed to occur at early times, presumably because of the small density difference between the gravity current and lower ambient layer and in spite of the small value for Fr. Mixing by entrainment effectively increases the gravity current fluid volume above the value assumed in (4.3). On the other hand, there exist numerous cases that exhibit relatively little mixing but where $n_{\min}$ is likewise exceeded, now because the gravity current has significant downstream momentum. As shown by row 8 (excluding the header row) and, more especially, row 4 of table 4.1, the experiments associated with small S suggest front speeds large enough to leave troughs under-filled with gravity current fluid in contrast to the picture suggested by figure 4.12.

Table 4.1: Topographic peaks overcome by the gravity current front as a function of the lock depth (D/H), lock length ($L = 48.7\,\text{cm}$), and topographic profile (A/λ and A/H).

D/H	A/λ	A/H	$n_{\min}$ from (4.2) and (4.3)	$(n_{\min})_{\text{expt}}$	$(n_{\max})_{\text{expt}}$
0.5	0.083 ($\lambda = 24.0\,\text{cm}$)	0.11	7	≥ 5 [all S]	≥ 5 [all S]
0.75	0.083 ($\lambda = 24.0\,\text{cm}$)	0.11	12	≥ 5 [all S]	≥ 5 [all S]
1.0	0.083 ($\lambda = 24.0\,\text{cm}$)	0.11	16	≥ 5 [all S]	≥ 5 [all S]
0.5	0.167 ($\lambda = 24.0\,\text{cm}$)	0.25	2	2 [$S = 0.867$]	≥ 5 [$S = 0.177$]
0.75	0.167 ($\lambda = 24.0\,\text{cm}$)	0.25	4	≥ 5 [all S]	≥ 5 [all S]
1.0	0.167 ($\lambda = 24.0\,\text{cm}$)	0.25	6	≥ 5 [all S]	≥ 5 [all S]
1.0	0.167 ($\lambda = 24.0\,\text{cm}$)	0.39	3	4 [all S]	4 [all S]
0.5	0.083 ($\lambda = 48.0\,\text{cm}$)	0.25	1	1 [$S = 0.872, 0.700$]	≥ 2 [$S < 0.700$]
0.75	0.083 ($\lambda = 48.0\,\text{cm}$)	0.25	2	≥ 2 [all S]	≥ 2 [all S]
1.0	0.083 ($\lambda = 48.0\,\text{cm}$)	0.25	3	≥ 2 [all S]	≥ 2 [all S]
1.0	0.083 ($\lambda = 48.0\,\text{cm}$)	0.39	2	≥ 2 [all S]	≥ 2 [all S]

Chapter 5

Summary and conclusions

An experimental investigation of gravity current flow over sinusoidal topography in a two-layer ambient was conducted for Boussinesq flow. The sinusoidal topographic profile is characterized by the ratio of topographic amplitude to the average channel depth, A/H and one-quarter the mean absolute slope, A/λ, while the initial conditions of each fluid are described by the fractional lock and interface heights D/H and h_1/H, respectively, alongside a density ratio, $S \equiv (\rho_1 - \rho_2)/(\rho_0 - \rho_2)$.

Analysis is facilitated using composite time-series (CTS) images that show the gravity current fluid height and the ambient interface deflection for all t and s. From CTS images, the average front speed is extracted and represented by a Froude number, Fr. Figures 4.1 and 4.3 show the variation of Fr with S, h_1/H, A/λ, and D/H. In general, Fr is observed to be a decreasing function of the first three of these parameters and an increasing function of the latter parameter. Surprisingly, Fr is little influenced by varying A/H – see figure 4.2.

As the gravity current fluid travels up- and downslope, it expe-

riences minor instantaneous changes in front speed (see figure 4.6), but most often, the gravity current maintains a relatively constant speed (see figure 4.5) despite large variations in the channel depth. This unexpected observation is attributed to the two competing influences of along-slope variations in the buoyancy force and contracting/expanding streamlines. These influences act opposite to one another in their propensity to accelerate and decelerate gravity current fluid.

Because the front speed is reasonably constant in most cases, it is possible to compare this measured quantity with the speed of the interfacial disturbance that is excited from the collapse and propagation of the lock fluid. Tan et al. (2011) found that a gravity current propagating over a horizontal boundary had a front speed that approximately matched the interfacial disturbance speed when $S = S_{\text{crit}} \simeq 0.75$, independent of the ambient interface height. In the presence of topography, it was determined that S_{crit} is decreased from its flat bottom value by an amount that depends much more on A/λ than on A/H. More specifically, figure 4.11 indicates that $S_{\text{crit}} \simeq 0.53$ for $A/\lambda = 0.083$ and $S_{\text{crit}} \simeq 0.37$ for $A/\lambda = 0.167$. Note that h_1/H again has a negligible influence on the value of S_{crit}.

In the horizontal bottom case of Tan et al. (2011), subcritical gravity currents were observed to be oftentimes drastically influenced by the interfacial disturbance. Here, by contrast, these disturbances play a less obvious role; often it was the shear flow at a topographic peak or the lack of momentum required to ascend a large slope that arrested the gravity current fluid. For example,

figure 4.7 shows an experiment where shear forces from the return flow of ambient fluid are the most influential factor in decelerating the gravity current. Shear forces are especially relevant because the Reynolds number, Re, for this particular experiment is comparatively small.

The shear forces acting on the gravity current also help to generate large Kelvin-Helmholtz vortices downstream of topographic peaks, much the same as the "intensive mixing vortices" observed by Tokyay et al. (2011). With the creation of a large Kelvin-Helmholtz vortex, there follows a large sloshing motion as the gravity current fluid relaxes back into the topographic troughs. The size of the Kelvin-Helmholtz vortices, and thus the severity of sloshing, prove difficult to predict based on initial and geometric conditions mainly because of the many vertical length scales and fluid velocities inherent in a three layer transient flow problem. In the long time limit, sloshing motions disappear due to dissipation and hence the interface between the dense gravity current fluid and the overlying ambient is horizontal. This horizontal interface between ρ_0 and ρ_1 coincides with the top of the topographic crests when D is small and S is large. Based on this observation, and assuming no mixing between the layers, a minimum number of topographic peaks overcome by each gravity current can be determined using (4.2) and (4.3). Table 4.1 shows the calculated minimum number of peaks along with the associated experimental values. Results show that the corresponding minimum number of peaks overcome will always be realized given enough time but can be surpassed when there

is substantial mixing and/or when S is small so that the gravity current has more significant inertia.

Future investigations could expand upon the present inquiry by developing a more quantitative model that predicts how far a gravity current will eventually travel downstream by incorporating S and by parameterizing entrainment/detrainment in some physically-meaningful fashion. This would be a difficult undertaking, however, because characterizing mixing in gravity currents remains a challenge even for the simple horizontal boundary case (Borden & Meiburg, 2013). Moreover, exploring this problem experimentally would require infrastructural upgrades in the form of a longer experimental tank in order to simultaneously preserve a high Reynolds number (sufficient gravity current height) and achieve a gravity current that is fully arrested by topography. Not to mention, it would also require a not insignificant amount of fabrication in order to obtain the corresponding long topography. Other novel investigations including a stratified ambient might mimic naturally occurring topographic profiles like specific oceanic bedforms or mountain ranges as the bottom boundary. Results from such investigations could, of course, be compared against the foundational results summarized here and also against related investigations such as Farmer & Armi (1985, 1986). Farmer & Armi's studies considered similitude examination of stratified flow over realistic topography, albeit in the context of a steady exchange flow.

Bibliography

Armi, L. 1986 The hydraulics of two flowing layers with different densities. *J. Fluid Mech.* **163**, 27–58.

Baines, P. G. 1995 *Topographic Effects in Stratified Flows*. Cambridge, England: Cambridge University Press.

Benjamin, T. B. 1968 Gravity currents and related phenomena. *J. Fluid Mech.* **31**, 209–248.

Bonnecaze, R. T. & Lister, J. R. 1999 Particle-driven gravity currents down planar slopes. *J. Fluid Mech.* **390**, 75–91.

Borden, Z. & Meiburg, E. 2013 Circulation based models for Boussinesq gravity currents. *Phys. Fluids* **25**, 101301.

Britter, R. E. & Linden, P. F. 1980 The motion of the front of a gravity current travelling down an incline. *J. Fluid Mech.* **99**, 531–542.

Farmer, D. M. & Armi, L. 1985 The internal hydraulics of the Strait of Gibraltar and associated sills and narrows. *Oceanologica Acta* **8**, 37–46.

Farmer, D. M. & Armi, L. 1986 Maximal two-layer exchange over a sill and through the combination of a sill and contraction with barotropic flow. *J. Fluid Mech.* **164**, 53–76.

Flury, M. & Gimmi, T. 2002 *Methods of Soil Analysis, Part 4, Physical Methods*. Madison, WI: Soil Science Society of America.

Gonzalez-Juez, E. & Meiburg, E. 2009 Shallow-water analysis of gravity-current flows past isolated obstacles. *J. Fluid Mech.* **635**, 415–438.

Gonzalez-Juez, E., Meiburg, E. & Constantinescu, G. 2009 Gravity currents impinging on bottom-mounted square cylinders: Flow fields and associated forces. *J. Fluid Mech.* **631**, 65–102.

Hatcher, L., Hogg, A. J. & Woods, A. W. 2000 The effects of drag on turbulent gravity currents. *J. Fluid Mech.* **416**, 297–314.

Hogg, A. J. & Woods, A. W. 2001 The transition from inertia- to bottom-drag-dominated motion of turbulent gravity currents. *J. Fluid Mech.* **449**, 201–224.

Hu, P. 2000 Diffusion coefficients of hydrologic tracers as measured by a Taylor dispersion apparatus. Master's thesis, New Mexico Inst. of Mining and Tech.

Huppert, H. E. & Simpson, J. E. 1980 The slumping of gravity currents. *J. Fluid Mech.* **99**, 785–799.

Kaye, N. B., Flynn, M. R., Cook, M. J. & Ji, Y. 2010 The role of diffusion on the interface thickness in a ventilated filling box. *J. Fluid Mech.* **652**, 195–205.

Lane-Serff, G. F., Beal, L. M. & Hadfield, T. D. 1995 Gravity current flow over obstacles. *J. Fluid Mech.* **292**, 39–53.

Marleau, L. J., Flynn, M. R. & Sutherland, B. R. 2014 Gravity currents propagating up a slope. *Phys. Fluids* **26**, 046605.

Maxworthy, T., Leilich, J., Simpson, J. & Meiburg, E. H. 2002 The propagation of a gravity current in a linearly stratified fluid. *J. Fluid Mech.* **453**, 371–394.

Nogueira, H., Adduce, C., Alves, E. & Franca, J. 2013 Analysis of lock-exchange gravity currents over smooth and rough beds. *Journal of Hydraulic Research* **51:4,**, 417–431.

Özgökmen, T. M. & Fischer, P. F. 2008 On the role of bottom roughness in overflows. *Ocean Modelling* **20**, 336–361.

Özgökmen, T. M., Fischer, P. F., Duan, J. & Iliescu, T. 2004 Entrainment in bottom gravity currents over complex topography from three-dimensional nonhydrostatic simulations. *Geophys. Res. Lett.* **31**, L13212.

Pawlak, G. & Armi, L. 2000 Mixing and entrainment in developing stratified currents. *J. Fluid Mech.* **424**, 45–73.

Rottman, J. W. & Simpson, J. E. 1983 Gravity currents produced by instantaneous releases of a heavy fluid in a rectangular channel. *J. Fluid Mech.* **135**, 95–110.

Sahuri, R. M., Kaminski, A. K., Flynn, M. R. & Ungarish, M. 2015 Axisymmetric gravity currents in two-layer density-stratified media. *Env. Fluid Mech.* p. in press.

Shin, J. O., Dalziel, S. B. & Linden, P. F. 2004 Gravity currents produced by lock exchange. *J. Fluid Mech.* **521**, 1–34.

Simpson, J. E. 1997 *Gravity Currents*, 2nd edn. Cambridge, England: Cambridge University Press.

Smeed, D. A. 2000 Hydraulic control of three-layer exchange flows: Application to the Bab al Mandab. *J. Phys. Oceanogr.* **30**, 2574–88.

Spiegel, E. A. & Veronis, G. 1960 On the Boussinesq approximation for a compressible fluid. *Astrophys. J.* **131**, 442–447.

Tan, A. W. 2010 Gravity currents in two-layer stratified media. Master's thesis, Univ. of Alberta.

Tan, A. W., Nobes, D. S., Fleck, B. A. & Flynn, M. R. 2011 Gravity currents in two-layer stratified media. *Environ. Fluid Mech.* **11(2)**, 203–224 (DOI: 10.1007/s10652–010–9174–z).

Tokyay, T., Constantinescu, G. & Meiburg, E. 2011 Lock-exchange gravity currents with a high volume of release propagating over a periodic array of obstacles. *J. Fluid Mech.* **672**, 570–605.

Tokyay, T., Constantinescu, G. & Meiburg, E. 2014 Lock-exchange gravity currents with a low volume of release propagating over an array of obstacles. *J. Geophys. Res.-Oceans* **119**, 2752–2768.

Ungarish, M. 2006 On gravity currents in a linearly stratified ambient: A generalization of Benjamin's steady-state propagation results. *J. Fluid Mech.* **548**, 49–68.

Ungarish, M. 2009 *An Introduction to Gravity Currents and Intrusions*. Boca Raton, FL, USA: CRC Press.

von Kármán, T. 1940 The engineer grapples with nonlinear problems. *Bull. Am. Math. Soc.* **46**, 615–683.

White, B. L. & Helfrich, K. R. 2008 Gravity currents and internal waves in a stratified fluid. *J. Fluid Mech.* **616**, 327–356.

White, B. L. & Helfrich, K. R. 2012 A general description of a gravity current front propagating in a two-layer stratified fluid. *J. Fluid Mech.* **711**, 545–575.

Yih, C.-S. 1965 *Dynamics of Nonhomogeneous Fluids*. New York: Macmillan.

Appendices

Appendix A

Full-depth lock release experiments

Table A.1 gives a comprehensive summary of the data collected as part of experimental runs for full-depth lock-release experiments of the type described §3.1.1. More specifically, and for each experimental run, the values of the following parameters are specified: A/λ, A/H, D/H, h_1/H, and S. Also identified is whether the flow is approximately subcritical, critical, or supercritical and the resulting values of Fr, Ri, Re, lo/D, and n. Table A.2 gives the same information (except columns for n and the flow classification) for the runs used to create figure 4.2.

Table A.1: Complete experimental data for the full-depth lock-release experiments (except those reported in table A.2). Dashes in the last column indicate a uniform ambient with $S = 0$.

Run	A/λ	A/H	D/H	h_1/H	S	Fr	Ri	Re	lo/D	n	Flow classification
1	0.083	0.11	1	1	0	0.376	0.98	15,018	0.29	≥ 5	-
2	0.083	0.12	1	1	0	0.381	0.95	17,444	0.47	≥ 5	-
3	0.083	0.11	1	0.22	0.158	0.410	0.70	25,929	0.32	≥ 5	supercritical
4	0.083	0.12	1	0.24	0.297	0.384	0.66	20,593	0.34	≥ 5	supercritical
5	0.083	0.11	1	0.21	0.532	0.385	0.44	23,541	0.30	≥ 5	critical
6	0.083	0.12	1	0.25	0.690	0.360	0.33	20,155	0.28	≥ 5	subcritical
7	0.083	0.12	1	0.25	0.889	0.314	0.15	16,785	0.18	≥ 5	subcritical
8	0.083	0.12	1	0.45	0.211	0.373	0.78	21,068	0.34	≥ 5	supercritical
9	0.083	0.12	1	0.50	0.472	0.339	0.63	19,169	0.39	≥ 5	supercritical
10	0.083	0.12	1	0.50	0.539	0.336	0.56	19,570	0.37	≥ 5	supercritical
11	0.083	0.12	1	0.50	0.550	0.299	0.69	16,763	0.34	≥ 5	critical
12	0.083	0.12	1	0.49	0.654	0.290	0.57	16,535	0.31	≥ 5	subcritical
13	0.083	0.12	1	0.50	0.699	0.248	0.67	15,443	0.24	≥ 5	subcritical
14	0.083	0.12	1	0.51	0.731	0.273	0.50	16,040	0.21	≥ 5	subcritical
15	0.083	0.12	1	0.73	0.244	0.352	0.84	20,266	0.30	≥ 5	supercritical
16	0.083	0.12	1	0.75	0.443	0.325	0.73	18,372	0.42	≥ 5	supercritical
17	0.083	0.12	1	0.75	0.546	0.285	0.77	16,183	0.32	≥ 5	critical
18	0.083	0.12	1	0.74	0.744	0.211	0.79	11,802	0.42	≥ 5	subcritical
19	0.083	0.12	1	0.72	0.886	0.143	0.77	8,314	0.24	≥ 5	subcritical
20	0.167	0.25	1	1	0	0.374	0.84	11,629	0.41	≥ 5	-
21	0.167	0.24	1	0.50	0.227	0.355	0.73	16,595	0.37	≥ 5	supercritical
22	0.167	0.24	1	0.50	0.404	0.307	0.75	14,801	0.55	≥ 5	critical
23	0.167	0.24	1	0.51	0.527	0.301	0.62	14,478	0.50	≥ 5	subcritical
24	0.167	0.24	1	0.50	0.534	0.307	0.59	14,566	0.63	≥ 5	subcritical
25	0.167	0.24	1	0.51	0.612	0.276	0.60	14,033	0.46	≥ 5	subcritical
26	0.167	0.24	1	0.51	0.732	0.242	0.54	12,557	0.39	≥ 5	subcritical
27	0.167	0.24	1	0.51	0.869	0.199	0.39	11,409	0.19	≥ 5	subcritical
28	0.167	0.24	1	0.76	0.201	0.357	0.74	16,402	0.57	≥ 5	supercritical
29	0.167	0.24	1	0.76	0.499	0.274	0.79	13,190	0.48	≥ 5	subcritical
30	0.167	0.24	1	0.76	0.633	0.242	0.74	11,563	0.49	≥ 5	subcritical
31	0.167	0.24	1	0.75	0.710	0.197	0.88	9,412	0.47	≥ 5	subcritical
32	0.167	0.25	1	0.75	0.889	0.119	0.93	5,771	0.21	≥ 5	subcritical
33	0.167	0.36	1	1	0	0.369	0.74	6,809	0.51	4	-
34	0.167	0.39	1	0.77	0.210	0.362	0.58	7,160	0.35	4	supercritical
35	0.167	0.38	1	0.75	0.359	0.334	0.55	7,119	0.24	4	critical
36	0.167	0.37	1	0.75	0.570	0.254	0.66	7,212	0.41	4	subcritical
37	0.167	0.37	1	0.76	0.783	0.178	0.68	4,544	0.38	4	subcritical
38	0.083	0.24	1	1	0	0.453	0.58	15,032	0.49	≥ 2	-
39	0.083	0.25	1	0.49	0.208	0.406	0.56	19,132	0.46	≥ 2	supercritical
40	0.083	0.25	1	0.50	0.376	0.365	0.55	17,889	0.50	≥ 2	supercritical
41	0.083	0.25	1	0.50	0.525	0.327	0.52	16,305	0.49	≥ 2	supercritical
42	0.083	0.24	1	0.50	0.556	0.333	0.47	16,374	0.48	≥ 2	supercritical
43	0.083	0.25	1	0.50	0.715	0.289	0.40	13,396	0.43	≥ 2	subcritical
44	0.083	0.25	1	0.50	0.875	0.234	0.27	11,277	0.18	≥ 2	subcritical
45	0.083	0.25	1	0.75	0.181	0.406	0.58	19,817	0.48	≥ 2	supercritical
46	0.083	0.25	1	0.75	0.367	0.361	0.57	17,896	0.44	≥ 2	supercritical
47	0.083	0.25	1	0.75	0.533	0.297	0.62	14,630	0.28	≥ 2	supercritical
48	0.083	0.25	1	0.75	0.716	0.241	0.57	11,644	0.49	≥ 2	subcritical
49	0.083	0.25	1	0.75	0.873	0.169	0.52	8,035	0.52	≥ 2	subcritical
50	0.083	0.38	1	1	0	0.414	0.56	7,410	0.64	≥ 2	-
51	0.083	0.39	1	0.75	0.094	0.357	0.67	9,309	0.57	≥ 2	supercritical
52	0.083	0.37	1	0.76	0.366	0.316	0.62	9,273	0.48	≥ 2	supercritical
53	0.083	0.38	1	0.76	0.551	0.269	0.60	7,301	0.34	≥ 2	supercritical
54	0.083	0.38	1	0.76	0.700	0.256	0.44	6,852	0.54	≥ 2	subcritical
55	0.083	0.38	1	0.76	0.890	0.137	0.57	3,558	0.23	≥ 2	subcritical

Table A.2: Experimental data for the runs reported in figure 4.2.

Run	A/λ	A/H	D/H	h_1/H	S	Fr	Ri	Re	ℓ_0/D
92	0.167	0.196	1	0.50	0.515	0.317	0.61	21,175	0.41
93	0.167	0.220	1	0.49	0.526	0.304	0.63	17,783	0.39
26	0.167	0.240	1	0.51	0.527	0.301	0.62	14,478	0.50
94	0.167	0.282	1	0.49	0.523	0.305	0.58	11,977	0.54
95	0.167	0.328	1	0.50	0.512	0.304	0.56	9,258	0.59

Appendix B

Partial-depth lock release experiments

Table B.1 gives a comprehensive summary of the data collected as part of experimental runs for partial-depth lock-release experiments of the type described §3.1.2. More specifically, and for each experimental run, the values of the following parameters are specified: A/λ, A/H, D/H, h_1/H, and S. Also identified is whether the flow is approximately subcritical, critical, or supercritical and the resulting values of Fr, Ri, Re, lo/D, and n.

Table B.1: Complete experimental data for the partial-depth lock-release experiments. Dashes in the last column indicate a uniform ambient with $S = 0$.

Run	A/λ	A/H	D/H	h_1/H	S	Fr	Ri	Re	lo/D	n	flow classification
56	0.083	0.12	0.489	1	0	0.369	1.02	7,656	0.59	≥ 5	-
57	0.083	0.12	0.490	0.51	0.193	0.352	0.90	9,933	0.66	≥ 5	supercritical
58	0.083	0.12	0.507	0.50	0.376	0.325	0.82	9,642	0.43	≥ 5	supercritical
59	0.083	0.12	0.502	0.51	0.538	0.261	0.94	7,733	0.34	≥ 5	subcritical
60	0.083	0.12	0.504	0.50	0.703	0.162	1.56	4,997	0.39	≥ 5	subcritical
61	0.083	0.12	0.502	0.49	0.878	0.092	1.99	2,433	0.27	≥ 5	subcritical
62	0.083	0.12	0.731	1	0	0.399	0.87	11,915	0.65	≥ 5	-
63	0.083	0.12	0.732	0.50	0.204	0.396	0.70	16,717	0.57	≥ 5	supercritical
64	0.083	0.12	0.746	0.50	0.361	0.340	0.76	14,538	0.49	≥ 5	supercritical
65	0.083	0.12	0.746	0.50	0.509	0.345	0.57	14,721	0.45	≥ 5	supercritical
66	0.083	0.12	0.737	0.51	0.707	0.288	0.49	12,218	0.26	≥ 5	subcritical
67	0.083	0.12	0.742	0.51	0.878	0.191	0.46	8,266	0.10	≥ 5	subcritical
68	0.167	0.24	0.470	1	0	0.333	1.07	6,301	0.51	4	-
69	0.167	0.24	0.493	0.50	0.177	0.311	1.00	7,492	0.54	≥ 5	supercritical
70	0.167	0.25	0.488	0.49	0.348	0.291	0.91	6,990	0.32	4	critical
71	0.167	0.24	0.502	0.50	0.532	0.242	0.95	5,308	0.47	3	subcritical
72	0.167	0.24	0.501	0.49	0.709	0.183	1.03	4,159	0.38	2	subcritical
73	0.167	0.25	0.502	0.50	0.867	0.103	1.47	2,883	0.24	2	subcritical
74	0.167	0.23	0.711	1	0	0.377	0.84	1,0751	0.53	≥ 5	-
75	0.167	0.24	0.728	0.50	0.203	0.367	0.70	12,657	0.48	≥ 5	supercritical
76	0.167	0.25	0.735	0.49	0.350	0.344	0.65	11,673	0.64	≥ 5	critical
77	0.167	0.24	0.750	0.50	0.535	0.291	0.65	10,515	0.56	≥ 5	subcritical
78	0.167	0.24	0.737	0.49	0.712	0.217	0.72	8,889	0.41	≥ 5	subcritical
79	0.167	0.25	0.740	0.49	0.874	0.163	0.56	5,818	0.28	≥ 5	subcritical
80	0.083	0.26	0.521	1	0	0.426	0.64	8,605	0.84	≥ 2	-
81	0.083	0.25	0.485	0.52	0.199	0.378	0.66	9,776	0.56	≥ 2	supercritical
82	0.083	0.25	0.498	0.50	0.350	0.366	0.57	9,220	0.75	≥ 2	supercritical
83	0.083	0.25	0.487	0.49	0.517	0.237	1.01	5,615	0.37	≥ 2	critical
84	0.083	0.25	0.486	0.50	0.700	0.147	1.62	3,456	0.56	1	subcritical
85	0.083	0.25	0.489	0.50	0.872	0.064	3.68	1,666	0.19	1	subcritical
86	0.083	0.25	0.738	1	0	0.456	0.56	13,111	0.58	≥ 2	-
87	0.083	0.25	0.718	0.50	0.181	0.437	0.51	15,765	0.68	≥ 2	supercritical
88	0.083	0.25	0.741	0.50	0.357	0.395	0.48	14,296	0.63	≥ 2	supercritical
89	0.083	0.25	0.732	0.50	0.529	0.313	0.56	11,158	0.64	≥ 2	critical
90	0.083	0.25	0.729	0.50	0.711	0.261	0.50	8,957	0.37	≥ 2	subcritical
91	0.083	0.25	0.726	0.50	0.868	0.189	0.43	5,664	0.45	≥ 2	subcritical

Appendix C

Richardson number

The Richardson number can be used to characterize the stability of a density-stratified shear flow. Here, we wish to assess the stability of the interface between the gravity current and the ambient at a location upstream of the gravity current head. In the present context, this task is made considerably more difficult by the fact that the ambient is comprised of two layers. To simplify the present analysis, we regard the ambient as having a single density equal to the density of the lower layer. Thus our definition of the Richardson number reads as follows:

$$\mathrm{Ri} \equiv \frac{g'_{10} d}{(\Delta U)^2} \tag{C.1}$$

where $g'_{10} = g\frac{\rho_1 - \rho_0}{\rho_0}$ is the reduced gravity based on the density difference between the gravity current and the lower ambient layer, ΔU is the velocity difference between these two layers, and d is the thickness of the velocity interface. At the topographic peak, the analysis of Farmer & Armi (1986) suggests that maximal exchange occurs when the lower layer has a steady-state depth of $3/8^{\mathrm{ths}}$ of the smallest channel depth. Given this result and assuming (i) the flow

speeds in each layer are uniform, (ii) the flow behind the gravity current head becomes quasi-steady at the location of the crest, and (iii) the flow speed behind the head is approximately the same as the average gravity current front speed, $\bar{U}$, then ΔU can be estimated as $\Delta U = 1.6\bar{U}$. The thickness of the velocity interface behind the gravity current head is difficult to quantify; an analytical model that predicts d has yet to be developed even in the absence of bottom topography. We therefore estimate d based on the figure 9 empirical results of gravity currents propagating over a horizontal boundary from Borden & Meiburg (2013). The vertical length scale of the mixing region is then chosen as 40% of the smallest channel depth, $0.4(H - A)$. On these bases, (C.1) can be modified to read

$$\mathrm{Ri} = g'_{10}\frac{0.4(H-A)}{(1.6\bar{U})^2} \tag{C.2}$$

or equivalently,

$$\mathrm{Ri} = \Big(\frac{0.15625}{\mathrm{Fr}^2}\Big)(1-S)(1-\frac{A}{H}) \tag{C.3}$$

As discussed in §4.2, this definition of Ri provides discouragingly poor correlation with the resulting Kelvin-Helmholtz votex size. An attempt was made to improve the correlation using different veritcal length scales in (C.2) instead of $0.4(H - A)$ with limited success. The different length scales attempted include h_1, A, D, $h_1 - A$, and $h_1 - A + (1 - S)(h_2)$.

Appendix D

Ambient interface thickness

The figure 10 of Tan et al. (2011) suggests that the interface thickness has a minor impact on the front speed, at least in the case of no topography. The transition distance between the two ambient layer densities is a result of molecular diffusion and mixing as fluid of density ρ_2 is introduced during the filling of the tank. Because dye and salt have different diffusion coefficients, the interface thickness of one vs. the other will depend on the relative amount of diffusion vs. mixing. If the interface thickness is solely due to entrainment, the relatively slow process of diffusion will have little influence; therefore, both salt and dye will have similar interface thicknesses. Because the diffusion coefficient of salt, D_{salt}, is greater than that of dye, D_{dye}, the most conservative approach is to assume that the interface thickness depends only on diffusion. This assumption will result in the greatest discrepancy between the interface thickness of salt, δ_{salt}, and the interface thickness of dye, δ_{dye}, with the latter being much easier to measure. Following the analysis of Kaye et al. (2010), the molecular diffused distance, δ, varies with time, t, according to

$$\delta_i \sim (4D_i t)^{1/2} \tag{D.1}$$

The diffusion coefficient of Brilliant Blue FCF dye is reported by Hu (2000) to be $D_{dye} = 568\,\frac{\mu m^2}{s}$ while the diffusion coefficient of salt is $D_{salt} = 1611\,\frac{\mu m^2}{s}$ (Flury & Gimmi, 2002). The ratio of the two interface thicknesses is then

$$\frac{\delta_{salt}}{\delta_{dye}} = \sqrt{\frac{D_{salt}}{D_{dye}}} = 1.68 \tag{D.2}$$

Thus,

$$\delta_{salt} = 1.68\delta_{dye} \tag{D.3}$$

Note that δ_{dye} is easy to estimate by measuring the vertical variation of colour intensity in digitized experimental images as shown for six typical runs in figure D.1. Thus, using (D.3), it is straightforward to estimate δ_{salt}, which obviously has a much greater physical significance that δ_{dye}. By analyzing figure D.1, it can be concluded that δ_{dye} usually ranges from 10% - 15% of the channel depth. We can therefore state that $0.1H < \delta_{salt} < 0.25H$ with the upper bound being quite a conservative estimate. It is unlikely that the interface thickness ever reaches 25% of the channel depth because experiments were always run within a couple hours after starting to add the lower layer to the tank, i.e. based on (D.1) it is reasonable to expect most of the interface thickness to be a result of mixing, rather than of diffusion.

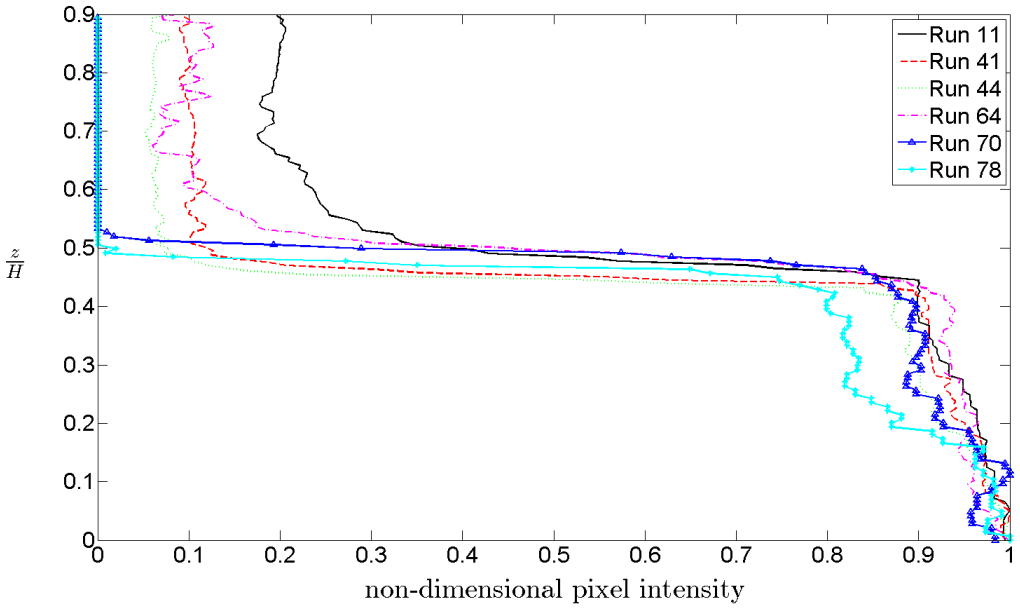

Figure D.1: Average channel height pixel intensities of experimental snapshots at $t = 0$ for 6 different runs used to estimate δ_{dye}. All runs have a target interface height of $h_1/H = 0.5$. Data were collected by averaging pixel intesity values over 6 different horizontal positions at equal vertical heights and normalized using the largest overall value collected from each snapshot.